UCID- 18834

NUMERICAL ELECTROMAGNETICS CODE (NEC) - METHOD OF MOMENTS

PART II: PROGRAM DESCRIPTION - CODE

G. J. Burke
A. J. Poggio

January 1981

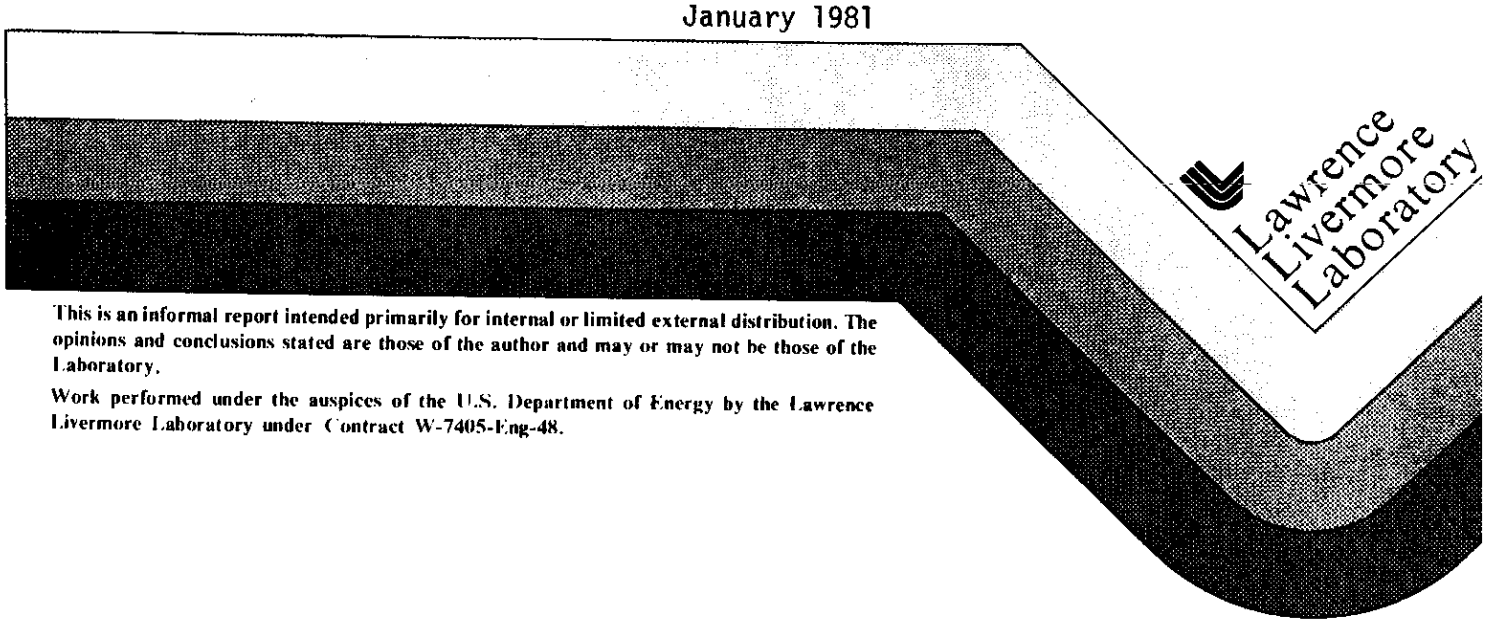

DISCLAIMER (From the original NEC document)

==========

The NEC2 documentation is composed of three sections

Part I: Program Description - Theory
Part II: Program Listing
Part III: User's guide

And may be obtained from the
National Technical Information Service (U.S. Department of Commerce)
5285 Port Royal Road
Springfield, VA 22161

Fax: +1 (703) 321 8547
Tel: +1 (703) 487 4679
`http://www.ntis.gov`

Ordering codes: AD-A075 209, AD-A075 289 and AD-A075 460 (not sure which is which)

==========

January 1997

This document (Part I) was scanned at a resolution of 196x204DPI and placed into a CCITT/G4 encoded PDF. Only minor cosmetic changes were made to the file. The left handed and right handed page data was recentered a bit. Some scanning noise, including punch holes, was eliminated. The scaling was chosen to (hopefully) make printing on DIN A4 paper possible.

I make no representation whatsoever as to the usefulness or exactitude of this Acrobat file, nor can have any responsibility for that of the original document.

Have fun!

Alexandre Kampouris, Montréal E-Mail: `ak@Radio-BIP.qc.ca`

Preface

The Numerical Electromagnetics Code (NEC) has been developed at the Lawrence Livermore Laboratory, Livermore, California, under the sponsorship of the Naval Ocean Systems Center and the Air Force Weapons Laboratory. It is an advanced version of the Antenna Modeling Program (AMP) developed in the early 1970's by MBAssociates for the Naval Research Laboratory, Naval Ship Engineering Center, U.S. Army ECOM/Communications Systems, U.S. Army Strategic Communications Command, and Rome Air Development Center under Office of Naval Research Contract N00014-71-C-0187. The present version of NEC is the result of efforts by G. J. Burke and A. J. Poggio of Lawrence Livermore Laboratory.

The documentation for NEC consists of three volumes:

Part I: NEC Program Description — Theory

Part II: NEC Program Description — Code

Part III: NEC User's Guide

The documentation has been prepared by using the AMP documents as foundations and by modifying those as needed. In some cases this led to minor changes in the original documents while in many cases major modifications were required.

Over the years many individuals have been contributors to AMP and NEC and are acknowledged here as follows:

R. W. Adams
J. N. Brittingham
G. J. Burke
F. J. Deadrick
K. K. Hazard
D. L. Knepp
D. L. Lager
R. J. Lytle
E. K. Miller
J. B. Morton
G. M. Pjerrou
A. J. Poggio
E. S. Selden

The support for the development of NEC-2 at the Lawrence Livermore Laboratory has been provided by the Naval Ocean Systems Center under MIPR-N0095376MP. Cognizant individuals under whom this project was carried out include: J. Rockway and J. Logan. Previous development of NEC also included the support of the Air Force Weapons Laboratory (Project Order 76-090) and was monitored by J. Castillo and TSgt. H. Goodwin.

Work was performed under the auspices of the U.S. Department of Energy under contract No. W-7405-Eng-48. Reference to a company or product name

does not imply approval or recommendation of the product by the University of California or the U.S. Department of Energy to the exclusion of others that may be suitable.

Contents

List of Illustrations

Section I
Introduction

The Numerical Electromagnetics Code (NEC-2) is a user-oriented computer code for the analysis of the electromagnetic response of antennas and other metal structures. It is built around the numerical solution of integral equations for the currents induced on the structure by sources or incident fields. This approach avoids many of the simplifying assumptions required by other solution methods and provides a highly accurate and versatile tool for electromagnetic analysis.

The code combines an integral equation for smooth surfaces with one specialized to wires to provide for convenient and accurate modeling of a wide range of structures. A model may include nonradiating networks and transmission lines connecting parts of the structure, perfect or imperfect conductors, and lumped-element loading. A structure may also be modeled over a ground plane that may be either a perfect or imperfect conductor.

The excitation may be either voltage sources on the structure or an incident plane wave of linear or elliptic polarization. The output may include induced currents and charges, near electric or magnetic fields, and radiated fields. Hence, the program is suited to either antenna analysis or scattering and EMP studies. NEC and its predecessor AMP have been used successfully to model a wide range of antennas including complex environments such as ships. Results from modeling several antennas with NEC are shown in refs. 36, 37, and 38 with measured data for comparison.

The integral-equation approach is best suited to structures with dimensions up to several wavelengths. Although there is no theoretical size limit, the numerical solution requires a matrix equation of increasing order as the structure size is increased relative to wavelength. Hence, modeling very large structures may require more computer time and file storage than is practical on a particular machine. In such cases standard high-frequency approximations such as geometrical or physical optics, or geometric theory of diffraction may be more suitable than the integral equation approach used in NEC.

The code NEC-2 is the latest in a series of electromagnetics codes, each of which has built upon the previous one. The first in the series was the code BRACT which was developed at MBAssociates in San Ramon, California, under the funding of the Air Force Space and Missiles Systems Organization (refs. 1 and 2). BRACT was specialized to scattering by arbitrary thin-wire configurations.

The code AMP followed BRACT and was developed at MBAssociates with funding from the Naval Research Laboratory, Naval Ship Engineering Center, U.S. Army ECOM/Communications Systems, U.S. Army Strategic Communications Command, and Rome Air Development Center under Office of Naval Research Contract N00014-71-C-0187. AMP uses the same numerical solution method as BRACT with the addition of the capability of modeling a structure over a ground plane and an option to use file storage to greatly increase the maximum structure size that may be modeled. The program input and output were extensively revised for AMP so that the code could be used with a minimum of learning and computer programming experience. AMP includes extensive documentation to aid in understanding, using, and modifying the code (refs. 3, 4 and 5).

A modeling option specialized to surfaces was added to the wire modeling capabilities of AMP in the AMP2 code (ref. 6). A simplified approximation for large interaction distances was also included in AMP2 to reduce running time for large structures.

The code NEC-1 added to AMP2 a more accurate current expansion along wires and at multiple wire junctions, and an option in the wire modeling technique for greater accuracy on thick wires. A new model for a voltage source was added and several other modifications made for increased accuracy and efficiency.

NEC-2 retains all features of NEC-1 except for a restart option. Major additions in NEC-2 are the Numerical Green's Function for partitioned-matrix solution and a treatment for lossy grounds that is accurate for antennas very close to the ground surface. NEC-2 also includes an option to compute maximum coupling between antennas and new options for structure input.

Part I of this document describes the equations and numerical methods used in NEC. Part III: NEC User's Guide (ref. 7) contains instructions for using the code, including preparation of input and interpretation of output. Part II: NEC Program Description — Code (ref. 8) describes the coding in detail. The user encountering the code for the first time should begin with the User's Guide and try modeling some simple antennas. Part II will be of interest mainly to someone attempting to modify the code. Reading part I will be useful to the new user of NEC-2, however, since an understanding of the theory and solution method will assist in the proper application of the code.

Section II
The Integral Equations For Free Space

The NEC program uses both an electric-field integral equation (EFIE) and a magnetic-field integral equation (MFIE) to model the electromagnetic response of general structures. Each equation has advantages for particular structure types. The EFIE is well suited for thin-wire structures of small or vanishing conductor volume while the MFIE, which fails for the thin-wire case, is more attractive for voluminous structures, especially those having large smooth surfaces. The EFIE can also be used to model surfaces and is preferred for thin structures where there is little separation between a front and back surface. Although the EFIE is specialized to thin wires in this program, it has been used to represent surfaces by wire grids with reasonable success for far-field quantities but with variable accuracy for surface fields. For a structure containing both wires and surfaces the EFIE and MFIE are coupled. This combination of the EFIE and MFIE was proposed and used by Albertsen, Hansen, and Jensen at the Technical University of Denmark (ref. 9) although the details of their numerical solution differ from those in NEC. A rigorous derivation of the EFIE and MFIE used in NEC is given by Poggio and Miller (ref. 10). The equations and their derivation are outlined in the following sections.

1. THE ELECTRIC FIELD INTEGRAL EQUATION (EFIE)

The form of the EFIE used in NEC follows from an integral representation for the electric field of a volume current distribution $\vec{J}$,

$$\vec{E}(\vec{r}) = \frac{-j\eta}{4\pi k} \int_v \vec{J}(\vec{r}') \cdot \overline{\overline{G}}(\vec{r}, \vec{r}')\, dV', \tag{1}$$

where

$$\overline{\overline{G}}(\vec{r}, \vec{r}') = (k^2\overline{\overline{I}} + \nabla\nabla)g(\vec{r}, \vec{r}'),$$

$$g(\vec{r}, \vec{r}') = \exp(-jk|\vec{r} - \vec{r}'|)/|\vec{r} - \vec{r}'|,$$

$$k = \omega\sqrt{\mu_o \varepsilon_o},$$

$$\eta = \sqrt{\mu_o/\varepsilon_o}$$

and the time convention is $\exp(j\omega t)$. $\overline{\overline{I}}$ is the identity dyad $(\hat{x}\hat{x} + \hat{y}\hat{y} + \hat{z}\hat{z})$. When the current distribution is limited to the surface of a perfectly conducting body, equation (1) becomes

$$\vec{E}(\vec{r}) = \frac{-j\eta}{4\pi k} \int_S \vec{J}_s(\vec{r}') \cdot \overline{\overline{G}}(\vec{r}, \vec{r}')\, dA', \tag{2}$$

with $\vec{J}_s$ the surface current density. The observation point $\vec{r}$ is restricted to be off the surface S so that $\vec{r} \neq \vec{r}'$.

If $\vec{r}$ approaches S as a limit, equation (2) becomes

$$\vec{E}(\vec{r}) = \frac{-j\eta}{4\pi k} \oint_S \vec{J}_s(\vec{r}') \cdot \overline{\overline{G}}(\vec{r}, \vec{r}')\, dA', \tag{3}$$

where the principal value integral, $\oint$, is indicated since $g(\vec{r}, \vec{r}')$ is now unbounded.

An integral equation for the current induced on S by an incident field $\vec{E}^I$ can be obtained from equation (3) and the boundary condition for $\vec{r} \in S$,

$$\hat{n}(\vec{r}) \times \left[\vec{E}^s(\vec{r}) + \vec{E}^I(\vec{r}) \right] = 0, \tag{4}$$

where $\hat{n}(\vec{r})$ is the unit normal vector of the surface at $\vec{r}$ and $\vec{E}^s$ is the field due to the induced current $\vec{J}_s$. Substituting equation (3) for $\vec{E}^s$ yields the integral equation,

$$-\hat{n}(\vec{r}) \times \vec{E}^I(\vec{r}) = \frac{-j\eta}{4\pi k} \hat{n}(\vec{r}) \times$$

$$\oint_S \vec{J}_s(\vec{r}') \cdot (k^2 \overline{\overline{I}} + \nabla\nabla) g(\vec{r}, \vec{r}')\, dA'. \tag{5}$$

The vector integral in equation (5) can be reduced to a scalar integral equation when the conducting surface S is that of a cylindrical thin wire, thereby making the solution much easier. The assumptions applied for a thin wire, known as the thin-wire approximation, are as follows:

a. Transverse currents can be neglected relative to axial currents on the wire.

b. The circumferential variation in the axial current can be neglected.

c. The current can be represented by a filament on the wire axis.

d. The boundary condition on the electric field need be enforced in the axial direction only.

These widely used approximations are valid as long as the wire radius is much less than the wavelength and much less than the wire length. An alternate kernel for the EFIE, based on an extended thin-wire approximation in which condition c is relaxed, is also included in NEC for wires having too large a radius for the thin-wire approximation (ref. 11).

From assumptions a, b and c, the surface current $\vec{J}_s(\vec{r})$ on a wire of radius a can be replaced by a filamentary current I where

$$I(s)\hat{s} = 2\pi a\vec{J}_s(\vec{r}),$$

s = distance parameter along the wire axis at $\vec{r}$, and

$\hat{s}$ = unit vector tangent to the wire axis at $\vec{r}$.

Equation (5) then becomes

$$-\hat{n}(\vec{r}) \times \vec{E}^I(\vec{r}) = \frac{-j\eta}{4\pi k}\,\hat{n}(\vec{r}) \times \int_L I(s')\left(k^2\hat{s}' - \nabla\frac{\partial}{\partial s'}\right) g(\vec{r}, \vec{r}')\, ds', \qquad (6)$$

where the integration is over the length of the wire. Enforcing the boundary condition in the axial direction reduces Eq. (6) to the scalar equation,

$$-\hat{s} \cdot \vec{E}^I(\vec{r}) = \frac{-j\eta}{4\pi k}\int_L I(s')\left(k^2\hat{s} \cdot \hat{s}' - \frac{\partial^2}{\partial s\partial s'}\right) g(\vec{r}, \vec{r}')\, ds'. \qquad (7)$$

Since $\vec{r}'$ is now the point at s' on the wire axis while $\vec{r}$ is a point at s on the wire surface $|\vec{r} - \vec{r}'| \geq a$ and the integrand is bounded.

2. THE MAGNETIC FIELD INTEGRAL EQUATION (MFIE)

The MFIE is derived from the integral representation for the magnetic field of a surface current distribution $\vec{J}_s$,

$$\vec{H}^s(\vec{r}) = \frac{1}{4\pi} \int_S \vec{J}_s(\vec{r}') \times \nabla' \, g(\vec{r}, \vec{r}') \, dA', \tag{8}$$

where the differentiation is with respect to the integration variable $\vec{r}'$. If the current $\vec{J}_s$ is induced by an external incident field $\vec{H}^I$, then the total magnetic field inside the perfectly conducting surface must be zero. Hence, for $\vec{r}$ just inside the surface S,

$$\vec{H}^I(\vec{r}) + \vec{H}^s(\vec{r}) = 0, \tag{9}$$

where $\vec{H}^I$ is the incident field with the structure removed, and $\vec{H}^s$ is the scattered field given by equation (8). The integral equation for $\vec{J}_s$ may be obtained by letting $\vec{r}$ approach the surface point $\vec{r}_o$ from inside the surface along the normal $\hat{n}(\vec{r}_o)$. The surface component of equation (9) with equation (8) substituted for $\vec{H}^s$ is then

$$-\hat{n}(\vec{r}_o) \times \vec{H}^I(\vec{r}_o) = \hat{n}(\vec{r}_o) \times \frac{1}{4\pi} \lim_{\vec{r} \to \vec{r}_o} \int_S \vec{J}_s(\vec{r}') \times \nabla' \, g(\vec{r}, \vec{r}') \, dA',$$

where $\hat{n}(\vec{r}_o)$ is the outward directed normal vector at $\vec{r}_o$. The limit can be evaluated by using a result of potential theory (ref. 12) to yield the integral equation

$$-\hat{n}(\vec{r}_o) \times \vec{H}^I(\vec{r}_o) = -\frac{1}{2} \vec{J}_s(\vec{r}_o) + \frac{1}{4\pi} \int_S \hat{n}(\vec{r}_o) \times \left[\vec{J}_s(\vec{r}') \times \nabla' \, g(\vec{r}_o, \vec{r}') \right] dA'. \tag{10}$$

For solution in NEC, this vector integral equation is resolved into two scalar equations along the orthogonal surface vectors $\hat{t}_1$ and $\hat{t}_2$ where

$$\hat{t}_1(\vec{r}_o) \times \hat{t}_2(\vec{r}_o) = \hat{n}(\vec{r}_o).$$

By using the identity $\vec{u} \cdot (\vec{v} \times \vec{w}) = (\vec{u} \times \vec{v}) \cdot \vec{w}$ and noting that $\hat{t}_1 \times \hat{n} = -\hat{t}_2$ and $\hat{t}_2 \times \hat{n} = \hat{t}_1$, the scalar equations can be written,

$$\hat{t}_2(\vec{r}_o) \cdot \vec{H}^I(\vec{r}_o) = -\frac{1}{2}\hat{t}_1(\vec{r}_o) \cdot \vec{J}_s(\vec{r}_o) - \frac{1}{4\pi}\oint_S \hat{t}_2(\vec{r}_o) \cdot \left[\vec{J}_s(\vec{r}') \times \nabla' g(\vec{r}_o, \vec{r}')\right] dA'; \quad (11)$$

$$-\hat{t}_1(\vec{r}_o) \cdot \vec{H}^I(\vec{r}_o) = -\frac{1}{2}\hat{t}_2(\vec{r}_o) \cdot \vec{J}_s(\vec{r}_o) + \frac{1}{4\pi}\oint_S \hat{t}_1(\vec{r}_o) \cdot \left[\vec{J}_s(\vec{r}') \times \nabla' g(\vec{r}_o, \vec{r}')\right] dA'. \quad (12)$$

These two components suffice since there is no normal component of equation (10).

3. THE EFIE-MFIE HYBRID EQUATION

Program NEC uses the EFIE for thin wires and the MFIE for surfaces. For a structure consisting of both wires and surfaces, $\vec{r}$ in equation (7) is restricted to the wires, with the integral for $\vec{E}^s(\vec{r})$, extending over the complete structure. The thin-wire form of the integral in equation (7) is used over wires while the more general form of equation (5) must be used on surfaces. Likewise, $\vec{r}_o$ is restricted to surfaces in equations (11) and (12), with the integrals for $\vec{H}^s(\vec{r})$ extending over the complete structure. On wires the integral is simplified by the thin-wire approximation. The resulting coupled integral equations are, for $\vec{r}$ on wire surfaces,

$$-\hat{s} \cdot \vec{E}^I(\vec{r}) = \frac{-j\eta}{4\pi k}\int_L I(s')\left(k^2 \hat{s} \cdot \hat{s}' - \frac{\partial^2}{\partial s \partial s'}\right) g(\vec{r},\vec{r}')\, ds' - \frac{j\eta}{4\pi k}\int_{S_1} \vec{J}_s(\vec{r}') \cdot \left[k^2 \hat{s} - \nabla' \frac{\partial}{\partial s}\right] g(\vec{r},\vec{r}')\, dA', \quad (13)$$

and for $\vec{r}$ on surfaces excluding wires

$$\hat{t}_2(\vec{r}) \cdot \vec{H}^I(\vec{r}) = -\frac{1}{4\pi}\,\hat{t}_2(\vec{r}) \cdot \int_L I(s')\left(\hat{s}' \times \nabla' g(\vec{r},\vec{r}')\right) ds'$$

$$-\frac{1}{2}\,\hat{t}_1(\vec{r}) \cdot \vec{J}_s(\vec{r}) -$$

$$\frac{1}{4\pi} \oint_{S_1} \hat{t}_2(\vec{r}) \cdot \left[\vec{J}_s(\vec{r}') \times \nabla' g(\vec{r},\vec{r}')\right] dA', \quad (14)$$

and

$$-\hat{t}_1(\vec{r}) \cdot \vec{H}^I(\vec{r}) = \frac{1}{4\pi}\,\hat{t}_1(\vec{r}) \cdot \int_L I(s')\left(\hat{s}' \times \nabla' g(\vec{r},\vec{r}')\right) ds'$$

$$-\frac{1}{2}\,\hat{t}_2(\vec{r}) \cdot \vec{J}_s(\vec{r}) +$$

$$\frac{1}{4\pi} \oint_{S_1} \hat{t}_1(\vec{r}) \cdot \left[\vec{J}_s(\vec{r}') \times \nabla' g(\vec{r},\vec{r}')\right] dA'. \quad (15)$$

The symbol $\int_L$ represents integration over wires while $\oint_{S_1}$ represents integration over surfaces excluding wires. The numerical method used to solve equations (13), (14) and (15) is described in section III.

Section III
Numerical Solution

The integral equations (13), (14), and (15) are solved numerically in NEC by a form of the method of moments. An excellent general introduction to the method of moments can be found in R. F. Harrington's book, Field Computation by Moment Methods (ref. 13). A brief outline of the method follows.

The method of moments applies to a general linear-operator equation,

$$Lf = e, \tag{16}$$

where f is an unknown response, e is a known excitation, and L is a linear operator (an integral operator in the present case). The unknown function f may be expanded in a sum of basis functions, f_j, as

$$f = \sum_{j=1}^{N} \alpha_j f_j \ . \tag{17}$$

A set of equations for the coefficients α_j are then obtained by taking the inner product of equation (16) with a set of weighting functions $\{w_i\}$,

$$\langle w_i, Lf \rangle = \langle w_i, e \rangle \qquad i = 1, \ldots N \ . \tag{18}$$

Due to the linearity of L equation (17) substituted for f yields,

$$\sum_{j=1}^{N} \alpha_j \langle w_i, Lf_j \rangle = \langle w_i, e \rangle \ , \qquad i = 1, \ldots N \ .$$

This equation can be written in matrix notation as

$$[G]\ [A] = [E] \ , \tag{19}$$

where

$$G_{ij} = \langle w_i, Lf_j \rangle \ ,$$

$$A_j = \alpha_j \ ,$$

$$E_i = \langle w_i, e \rangle \ .$$

The solution is then

$$[A] = [G]^{-1} [E] .$$

For the solution of equations (13), (14), and (15), the inner product is defined as

$$\langle f, g \rangle = \int_S f(\vec{r}) g(\vec{r}) dA ,$$

where the integration is over the structure surface. Various choices are possible for the weighting functions $\{w_i\}$ and basis functions $\{f_j\}$. When $w_i = f_i$, the procedure is known as Galerkin's method. In NEC the basis and weight functions are different, w_i being chosen as a set of delta functions

$$w_i(\vec{r}) = \delta(\vec{r} - \vec{r}_i) ,$$

with $\{\vec{r}_i\}$ a set of points on the conducting surface. The result is a point sampling of the integral equations known as the collocation method of solution. Wires are divided into short straight segments with a sample point at the center of each segment while surfaces are approximated by a set of flat patches or facets with a sample point at the center of each patch.

The choice of basis functions is very important for an efficient and accurate solution. In NEC the support of f_i is restricted to a localized subsection of the surface near $\vec{r}_i$. This choice simplifies the evaluation of the inner-product integral and ensures that the matrix G will be well conditioned. For finite N, the sum of f_j cannot exactly equal a general current distribution so the functions f_i should be chosen as close as possible to the actual current distribution. Because of the nature of the integral-equation kernels, the choice of basis function is much more critical on wires than on surfaces. The functions used in NEC are explained in the following sections.

1. CURRENT EXPANSION ON WIRES

Wires in NEC are modeled by short straight segments with the current on each segment represented by three terms — a constant, a sine, and a cosine. This expansion was first used by Yeh and Mei (ref. 14) and has been shown to provide rapid solution convergence (ref. 15 and 16). It has the added advantage that the fields of the sinusoidal currents are easily evaluated in closed form. The amplitudes of the constant, sine, and cosine terms are related such

that their sum satisfies physical conditions on the local behavior of current and charge at the segment ends. This differs from AMP where the current was extrapolated to the centers of the adjacent segments, resulting in discontinuities in current and charge at the segment ends. Matching at the segment ends improves the solution accuracy, especially at the multiple-wire junctions of unequal length segments where AMP extrapolated to an average length segment, often with inaccurate results.

The total current on segment number j in NEC has the form

$$I_j(s) = A_j + B_j \sin k(s-s_j) + C_j \cos k(s-s_j) \ , \qquad (20)$$

$$|s-s_j| < \Delta_j/2 \ ,$$

where s_j is the value of s at the center of segment j and Δ_j is the length of segment j. Of the three unknown constants A_j, B_j, and C_j, two are eliminated by local conditions on the current leaving one constant, related to the current amplitude, to be determined by the matrix equation. The local conditions are applied to the current and to the linear charge density, q, which is related to the current by the equation of continuity

$$\frac{\partial I}{\partial s} = - j\omega q \ . \qquad (21)$$

At a junction of two segments with uniform radius, the obvious conditions are that the current and charge are continuous at the junction. At a junction of two or more segments with unequal radii, the continuity of current is generalized to Kirchoff's current law that the sum of currents into the junction is zero. The total charge in the vicinity of the junction is assumed to distribute itself on individual wires according to the wire radii, neglecting local coupling effects. T. T. Wu and R. W. P. King (ref. 17) have derived a condition that the linear charge density on a wire at a junction, and hence $\partial I/\partial s$, is determined by

$$\left.\frac{\partial I(s)}{\partial s}\right|_{s \text{ at junction}} = \frac{Q}{\ell n\left(\frac{2}{ka}\right) - \gamma} \ , \qquad (22)$$

where a = wire radius,

$$k = 2\pi/\lambda \ ,$$

$\gamma = 0.5772$ (Euler's constant).

Q is related to the total charge in the vicinity of the junction and is constant for all wires at the junction.

At a free wire end, the current may be assumed to go to zero. On a wire of finite radius, however, the current can flow onto the end cap and hence be nonzero at the wire end. In one study of this effect, a condition relating the current at the wire end to the current derivative was derived (ref. 18). For a wire of radius a, this condition is

$$I(s)\Big|_{s \text{ at end}} = \frac{-(\hat{s}\cdot\hat{n}_c)}{k} \frac{J_1(ka)}{J_o(ka)} \frac{\partial I(s)}{\partial s}\Big|_{s \text{ at end}},$$

where J_o and J_1 are Bessel functions of order 0 and 1. The unit vector $\hat{n}_c$ is normal to the end cap. Hence, $\hat{s} \cdot \hat{n}_c$ is +1 if the reference direction, $\hat{s}$, is toward the end, and -1 if $\hat{s}$ is away from the end.

Thus, for each segment two equations are obtained from the two ends:

$$I_j(s_j \pm \Delta_j/2) = \frac{\pm 1}{k} \frac{J_1(ka_j)}{J_o(ka_j)} \frac{\partial I_j(s)}{\partial s}\Big|_{s = s_j \pm \Delta_j/2} \tag{23}$$

at free ends, and

$$\frac{\partial I_j(s)}{\partial s}\Big|_{s = s_j \pm \Delta_j/2} = \frac{Q_j^{\pm}}{\ell n\left(\frac{2}{ka_j}\right) - \gamma} \tag{24}$$

at junctions. Two additional unknowns Q_j^- and Q_j^+ are associated with the junctions but can be eliminated by Kirchoff's current equation at each junction. The boundary-condition equations provide the additional equation-per-segment to completely determine the current function of equation (20) for every segment.

To apply these conditions, the current is expanded in a sum of basis functions chosen so that they satisfy the local conditions on current and charge in any linear combination. A typical set of basis functions and their sum on a four segment wire are shown in figure 1. For a general segment i in figure 2, the i^{th} basis function has a peak on segment i and extends onto

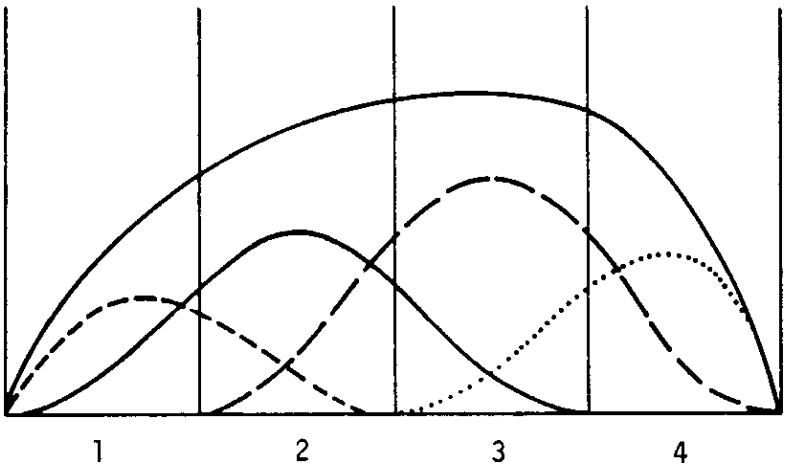

Figure 1. Current Basis Functions and Sum on a Four Segment Wire.

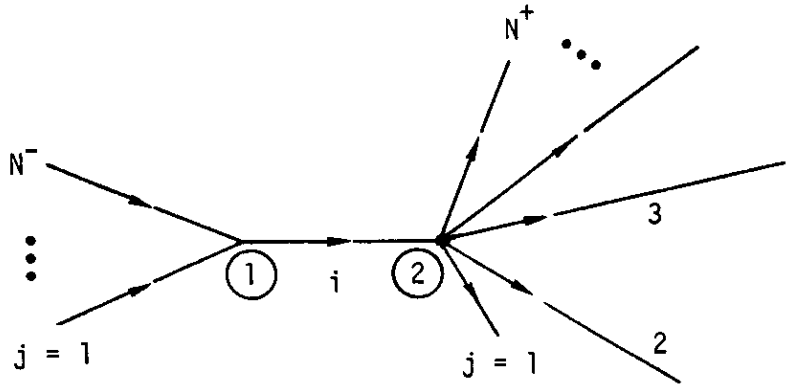

Figure 2. Segments Covered by the i^{th} Basis Function.

every segment connected to i, going to zero with zero derivative at the outer ends of the connected segments.

The general definition of the i^{th} basis function is given below. For the junction and end conditions described above, the following definitions apply for the factors in the segment end conditions:

$$a_i^- = a_i^+ = \left[\ell n \left(\frac{2}{ka_i} \right) - \gamma \right]^{-1} , \tag{25}$$

and

$$X_i = J_1(ka_i)/J_o(ka_i) .$$

The condition of zero current at a free end may be obtained by setting X_i to zero.

The portion of the i^{th} basis function on segment i is then

$$f_i^o(s) = A_i^o + B_i^o \sin k(s - s_i) + C_i^o \cos k(s - s_i) \qquad (26)$$

$$|s - s_i| < \Delta_i/2 \ .$$

If $N^- \neq 0$ and $N^+ \neq 0$, end conditions are

$$\frac{\partial}{\partial s} f_i^o(s) \Big|_{s = s_i - \Delta_i/2} = a_i^- Q_i^- \ , \qquad (27)$$

$$\frac{\partial}{\partial s} f_i^o(s) \Big|_{s = s_i + \Delta_i/2} = a_i^+ Q_i^+ \ . \qquad (28)$$

If $N^- = 0$ and $N^+ \neq 0$, end conditions are

$$f_i^o(s_i - \Delta_i/2) = \frac{1}{k} X_i \frac{\partial}{\partial s} f_i^o(s) \Big|_{s = s_i - \Delta_i/2} \qquad (29)$$

$$\frac{\partial}{\partial s} f_i^o(s) \Big|_{s = s_i + \Delta_i/2} = a_i^+ Q_i^+ \ . \qquad (30)$$

If $N^- \neq 0$ and $N^+ = 0$, end conditions are

$$\frac{\partial}{\partial s} f_i^o(s) \Big|_{s = s_i - \Delta_i/2} = a_i^- Q_i^- \ , \qquad (31)$$

$$f_i^o(s_i + \Delta_i/2) = \frac{-1}{k} X_i \frac{\partial}{\partial s} f_i^o(s) \Big|_{s = s_i + \Delta_i/2} \ . \qquad (32)$$

Over segments connected to end 1 of segment i, the i^{th} basis function is

$$f_j^-(s) = A_j^- + B_j^- \sin k(s - s_j) + C_j^- \cos k(s - s_j) \ . \qquad (33)$$

$$|s - s_j| < \Delta_j/2 \quad j = 1, \ \ldots \ , N^- \ .$$

End conditions are

$$f_j^-(s_j - \Delta_j/2) = 0 \ , \tag{34}$$

$$\frac{\partial}{\partial s} f_j^-(s) \Big|_{s = s_j - \Delta_j/2} = 0 \ , \tag{35}$$

$$\frac{\partial}{\partial s} f_j^-(s) \Big|_{s = s_j + \Delta_j/2} = a_j^+ Q_i^- \ . \tag{36}$$

Over segments connected to end 2 of segment i, the i^{th} basis function is

$$f_j^+(s) = A_j^+ + B_j^+ \sin k(s - s_j) + C_j^+ \cos k(s - s_j) \tag{37}$$

$$|s - s_j| < \Delta_j/2 \quad j = 1, \ \ldots \ , N^+ \ .$$

End conditions are

$$\frac{\partial}{\partial s} f_j^+(s) \Big|_{s = s_j - \Delta_j/2} = a_j^- Q_i^+ \ , \tag{38}$$

$$f_j^+(s_j + \Delta_j/2) = 0 \ , \tag{39}$$

$$\frac{\partial}{\partial s} f_j^+(s) \Big|_{s = s_j + \Delta_j/2} = 0 \ . \tag{40}$$

Equations (26), (33), and (37), defining the complete basis function, involve $3(N^- + N^+ + 1)$ unknown constants. Of these, $3(N^- + N^+) + 2$ unknowns are eliminated by the end conditions in terms of Q_i^- and Q_i^+ which can then be determined from the two Kirchoff's current equations:

$$\sum_{j=1}^{N^-} f_j^-(s_j + \Delta_j/2) = f_i^o(s_i - \Delta_i/2) \ , \text{ and} \tag{41}$$

$$\sum_{j=1}^{N^+} f_j^+(s_j - \Delta_j/2) = f_i^o(s_i + \Delta_i/2) \ . \tag{42}$$

The complete basis function is then defined in terms of one unknown constant. In this case A_i^o was set to -1 since the function amplitude is arbitrary, being determined by the boundary condition equations. The final result is given below:

$$A_j^- = \frac{a_j^+ Q_i^-}{\sin k \Delta_j} , \tag{43}$$

$$B_j^- = \frac{a_j^+ Q_i^-}{2 \cos k \Delta_j/2} , \tag{44}$$

$$C_j^- = \frac{- a_j^+ Q_i^-}{2 \sin k \Delta_j/2} , \tag{45}$$

$$A_j^+ = \frac{- a_j^- Q_i^+}{\sin k \Delta_j} , \tag{46}$$

$$B_j^+ = \frac{a_j^- Q_i^+}{2 \cos k \Delta_j/2} , \tag{47}$$

$$C_j^+ = \frac{a_j^- Q_i^+}{2 \sin k \Delta_j/2} . \tag{48}$$

For $N^- \neq 0$ and $N^+ \neq 0$,

$$A_i^o = - 1 , \tag{49}$$

$$B_i^o = \left(a_i^- Q_i^- + a_i^+ Q_i^+\right) \frac{\sin k \Delta_i/2}{\sin k \Delta_i} , \tag{50}$$

$$C_i^o = \left(a_i^- Q_i^- - a_i^+ Q_i^+\right) \frac{\cos k \Delta_i/2}{\sin k \Delta_i} , \tag{51}$$

$$Q_i^- = \frac{a_i^+(1 - \cos k\,\Delta_i) - P_i^+ \sin k\,\Delta_i}{\left(P_i^- P_i^+ + a_i^- a_i^+\right)\sin k\,\Delta_i + \left(P_i^- a_i^+ - P_i^+ a_i^-\right)\cos k\,\Delta_i} , \qquad (52)$$

$$Q_i^+ = \frac{a_i^-(\cos k\,\Delta_i - 1) - P_i^- \sin k\,\Delta_i}{\left(P_i^- P_i^+ + a_i^- a_i^+\right)\sin k\,\Delta_i + \left(P_i^- a_i^+ - P_i^+ a_i^-\right)\cos k\,\Delta_i} . \qquad (53)$$

For $N^- = 0$ and $N^+ \neq 0$,

$$A_i^o = -1 , \qquad (54)$$

$$B_i^o = \frac{\sin k\,\Delta_i/2}{\cos k\,\Delta_i - X_i \sin k\,\Delta_i} + a_i^+ Q_i^+ \frac{\cos k\,\Delta_i/2 - X_i \sin k\,\Delta_i/2}{\cos k\,\Delta_i - X_i \sin k\,\Delta_i} , \qquad (55)$$

$$C_i^o = \frac{\cos k\,\Delta_i/2}{\cos k\,\Delta_i - X_i \sin k\,\Delta_i} + a_i^+ Q_i^+ \frac{\sin k\,\Delta_i/2 + X_i \cos k\,\Delta_i/2}{\cos k\,\Delta_i - X_i \sin k\,\Delta_i} , \qquad (56)$$

$$Q_i^+ = \frac{\cos k\,\Delta_i - 1 - X_i \sin k\,\Delta_i}{\left(a_i^+ + X_i P_i^+\right)\sin k\,\Delta_i + \left(a_i^+ X_i - P_i^+\right)\cos k\,\Delta_i} \qquad (57)$$

For $N^- \neq 0$ and $N^+ = 0$,

$$A_i^o = -1 , \qquad (58)$$

$$B_i^o = \frac{-\sin k\,\Delta_i/2}{\cos k\,\Delta_i - X_i \sin k\,\Delta_i} + a_i^- Q_i^- \frac{\cos k\,\Delta_i/2 - X_i \sin k\,\Delta_i/2}{\cos k\,\Delta_i - X_i \sin k\,\Delta_i} , \qquad (59)$$

$$C_i^o = \frac{\cos k\,\Delta_i/2}{\cos k\,\Delta_i - X_i \sin k\,\Delta_i} - a_i^- Q_i^- \frac{\sin k\,\Delta_i/2 + X_i \cos k\,\Delta_i/2}{\cos k\,\Delta_i - X_i \sin k\,\Delta_i} , \qquad (60)$$

$$Q_i^- = \frac{1 - \cos k\,\Delta_i + X_i \sin k\,\Delta_i}{\left(a_i^- - X_i P_i^-\right)\sin k\,\Delta_i + \left(P_i^- + X_i a_i^-\right)\cos k\,\Delta_i} . \qquad (61)$$

For all cases,

$$P_i^- = \sum_{j=1}^{N^-} \left(\frac{1 - \cos k \Delta_j}{\sin k \Delta_j} \right) a_j^+ , \tag{62}$$

$$P_i^+ = \sum_{j=1}^{N^+} \left(\frac{\cos k \Delta_j - 1}{\sin k \Delta_j} \right) a_j^- , \tag{63}$$

where the sum for P_i^- is over segments connected to end 1 of segment i, and the sum for P_i^+ is over segments connected to end 2. If $N^- = N^+ = 0$, the complete basis function is

$$f_i^o = \frac{\cos k(s - s_i)}{\cos k \Delta_i/2 - X_i \sin \Delta_i/2} - 1 . \tag{64}$$

When a segment end is connected to a ground plane or to a surface modeled with the MFIE, the end condition on both the total current and the last basis function is

$$\frac{\partial}{\partial s} I_j(s) \Big|_{s = s_j \pm \Delta_j/2} = 0 ,$$

replacing the zero current condition at a free end. This condition does not require a separate treatment, however, but is obtained by computing the last basis function as if the last segment is connected to its image segment on the other side of the surface.

It should be noted that in AMP, the basis function f_i has unit value at the center of segment i and zero value at the centers of connected segments although it does extend onto the connected segments. As a result, the amplitude of f_i is the total current at the center of segment i. This is not true in NEC so the current at the center of segment i must be computed by summing the contributions of all basis functions extending onto segment i.

2. CURRENT EXPANSION ON SURFACES

Surfaces on which the MFIE is used are modeled by small flat patches. The surface current on each patch is expanded in a set of pulse functions except in the region of wire connection, as will be described later. The pulse function expansion for N_p patches is

$$\vec{J}_s(\vec{r}) = \sum_{j=1}^{N_p} (J_{1j}\ \hat{t}_{1j} + J_{2j}\ \hat{t}_{2j})\ V_j(\vec{r}) \ , \tag{65}$$

where

$$\hat{t}_{1j} = \hat{t}_1(\vec{r}_j) \ ,$$

$$\hat{t}_{2j} = \hat{t}_2(\vec{r}_j) \ ,$$

$\vec{r}_j$ = position of the center of patch number j ,

$V_j(\vec{r})$ = 1 for $\vec{r}$ on patch j and 0 otherwise.

The constants J_{1j} and J_{2j}, representing average surface-current density over the patch, are determined by the solution of the linear system of equations derived from the integral equations. The integrals for fields, due to the pulse basis functions, are evaluated numerically in a single step so that for integration, the pulses could be reduced to delta functions at the patch centers. That this simple approximation of the current yields good accuracy is one of the advantages of the MFIE for surfaces.

A more realistic representation of the surface current is needed, however, in the region where a wire connects to the surface. The treatment used in NEC, affecting the four coplanar patches about the connection point, is quite similar to that used by Albertsen et al. (ref. 9). In the region of the wire connection, the surface current contains a singular component due to the current flowing from the wire onto the surface. The total surface current should satisfy the condition,

$$\nabla_s \cdot \vec{J}_s(x,y) = J_o(x,y) + I_o\delta(x,y) \ ,$$

where the local coordinates x and y are defined in figure 3, ∇_s denotes surface divergence, $J_o(x,y)$ is a continuous function in the region ABCD, and I_o is the current at the base of the wire flowing onto the surface. One expansion which meets this requirement is

$$\vec{J}_s(x,y) = I_o\vec{f}(x,y) + \sum_{j=1}^{4} g_j(x,y)(\vec{J}_j - I_o\ \vec{f}_j) \ , \tag{66}$$

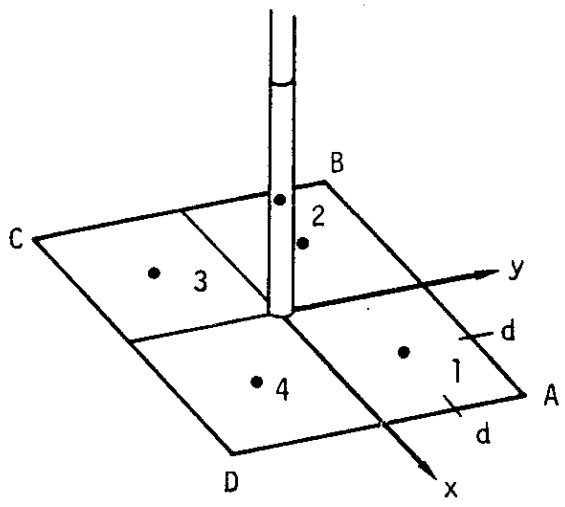

Figure 3. Detail of the Connection of a Wire to a Surface.

where

$$\vec{f}(x,y) = \frac{x\hat{x} + y\hat{y}}{2\pi(x^2 + y^2)} ,$$

$$\vec{J}_j = \vec{J}_s(x_j,y_j) ,$$

$$\vec{f}_j = \vec{f}(x_j,y_j) , \text{ and}$$

$(x_j,y_j) = (x,y)$ at the center of patch j. The interpolation functions $g_j(x,y)$ are chosen such that: $g_j(x,y)$ is differentiable on ABCD; $g_j(x_i,y_i) = \delta_{ij}$; and $\sum_{j=1}^{4} g_j(x,y) = 1$. The specific functions used in NEC are as follows:

$$g_1(x,y) = \frac{1}{4d^2}(d+x)(d+y) \qquad g_2(x,y) = \frac{1}{4d^2}(d-x)(d+y)$$

$$g_3(x,y) = \frac{1}{4d^2}(d-x)(d-y) \qquad g_4(x,y) = \frac{1}{4d^2}(d+x)(d-y)$$

Equation (66) is used when computing the electric field at the center of the connected wire segment due to the surface current on the four surrounding patches. In computing the field on any other segments or on any patches, the pulse-function form is used for all patches including those at the connection point. This saves integration time and is sufficiently accurate for the greater source to observation-point separations involved.

3. EVALUATION OF THE FIELDS

The current on each wire segment has the form

$$I_i(s) = A_i + B_i \sin k(s - s_i) + C_i \cos k(s - s_i) \qquad (67)$$

$$|s - s_i| < \Delta_i/2 ,$$

where $k = \omega\sqrt{\mu_o\varepsilon_o}$, and Δ_i is the segment length. The solution requires the evaluation of the electric field at each segment due to this current. Three

approximations of the integral equation kernel are used: a thin-wire form for most cases, an extended thin-wire form for thick wires, and a current element approximation for large interaction distances. In each case the evaluation of the field is greatly simplified by the use of formulas for the fields of the constant and sinusoidal current components.

The accuracy of the thin-wire approximation for a wire of radius a and length Δ depends on ka and Δ/a. Studies have shown that the thin-wire approximation leads to errors of less than 1% for Δ/a greater than 8 (ref. 11). Furthermore, in the numerical solution of the EFIE, the wire is divided into segments less than about 0.1λ in length to obtain an adequate representation of current distribution thus restricting ka to less than about 0.08. The extended thin-wire approximation is applicable to shorter and thicker segments, resulting in errors less than 1% for Δ/a greater than 2.

For the thin-wire kernel, the source current is approximated by a filament on the segment axis while the observation point is on the surface of the observation segment. The fields are evaluated with the source segment on the axis of a local cylindrical-coordinate system as illustrated in figure 4.

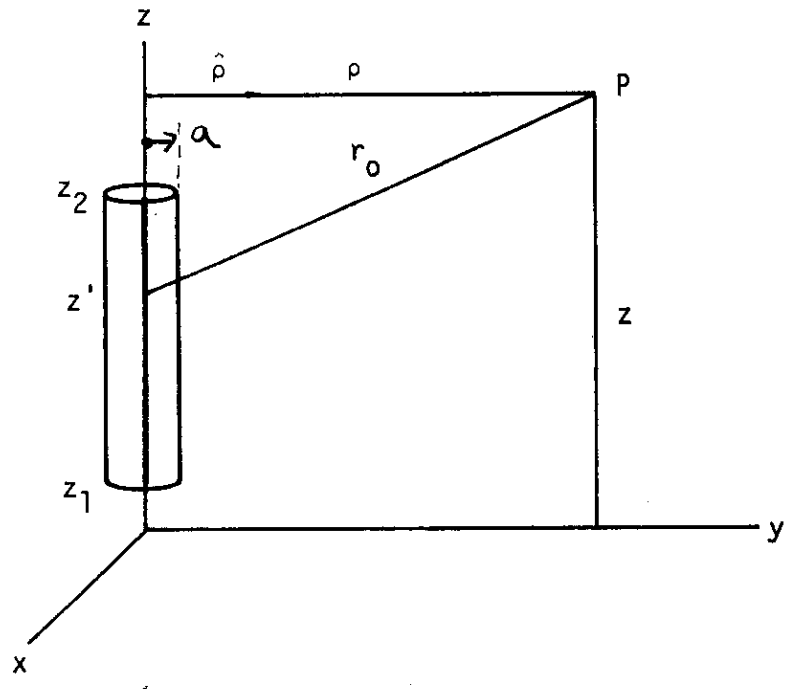

Figure 4. Current-Filament Geometry for the Thin-Wire Kernel.

Then with

$$G_o = \exp(-jkr_o)/r_o \ , \tag{68}$$

$$r_o = \left[\rho^2 + (z - z')^2\right]^{1/2} \ , \tag{69}$$

the ρ and z components of the electric field at P due to a sinusoidal current filament of arbitrary phase,

$$I = \sin(kz' - \Theta_o) \ , \ z_1 < z' < z_2 \ , \tag{70}$$

are

$$E_\rho^f(\rho,z) = \frac{-j\eta}{2k^2\lambda\rho}\left[(z'-z)\ I\ \frac{\partial G_o}{\partial z'} + I\ G_o - (z'-z)\ G_o\ \frac{\partial I}{\partial z'}\right]_{z_1}^{z_2} \ , \tag{71}$$

$$E_z^f(\rho,z) = \frac{j\eta}{2k^2\lambda}\left[G_o\ \frac{\partial I}{\partial z'} - I\ \frac{\partial G_o}{\partial z'}\right]_{z_1}^{z_2} \ . \tag{72}$$

For a current that is constant over the length of the segment with strength I, the fields are

$$E_\rho^f(\rho,z) = \frac{I}{\lambda}\ \frac{j\eta}{2k^2}\ \left[\frac{\partial G_o}{\partial \rho}\right]_{z_1}^{z_2} \ , \tag{73}$$

$$E_z^f(\rho,z) = -\frac{I}{\lambda}\ \frac{j\eta}{2k^2}\ \left\{\left[\frac{\partial G_o}{\partial z'}\right]_{z_1}^{z_2} + k^2 \int_{z_1}^{z_2} G_o\ dz'\right\} \ . \tag{74}$$

These field expressions are exact for the specified currents. The integral over z' of G_o is evaluated numerically in NEC.

Substituting sine and cosine currents and evaluating the derivatives yields the following equations for the fields. For

$$I = I_o \begin{pmatrix} \sin kz' \\ \cos kz' \end{pmatrix} , \tag{75}$$

$$E_\rho^f(\rho,z) = \frac{-I_o}{\lambda} \frac{j\eta}{2k^2\rho} G_o \left\{ k(z-z') \begin{pmatrix} \cos kz' \\ -\sin kz' \end{pmatrix} \right. \tag{76}$$

$$\left. + \left[1 - (z-z')^2 (1+jkr_o) \frac{1}{r_o^2} \right] \begin{pmatrix} \sin kz' \\ \cos kz' \end{pmatrix} \right\} \Bigg|_{z_1}^{z_2} ,$$

$$E_z^f(\rho,z) = \frac{I_o}{\lambda} \frac{j\eta}{2k^2} G_o \left\{ k \begin{pmatrix} \cos kz' \\ -\sin kz' \end{pmatrix} \right. \tag{77}$$

$$\left. - (1+jkr_o)(z-z') \frac{1}{r_o^2} \begin{pmatrix} \sin kz' \\ \cos kz' \end{pmatrix} \right\} \Bigg|_{z_1}^{z_2} .$$

For a constant current of strength I_o,

$$E_\rho^f(\rho,z) = - \frac{I_o}{\lambda} \frac{j\eta\rho}{2k^2} \left[(1+jkr_o) \frac{G_o}{r_o^2} \right]_{z_1}^{z_2} , \tag{78}$$

$$E_z^f(\rho,z) = - \frac{I_o}{\lambda} \frac{j\eta}{2k^2} \left\{ \left[(1+jkr_o)(z-z') \frac{G_o}{r_o^2} \right]_{z_1}^{z_2} \right. \tag{79}$$

$$\left. + k^2 \int_{z_1}^{z_2} G_o \, dz' \right\} .$$

Despite the seemingly crude approximation, the thin-wire kernel does accurately represent the effect of wire radius for wires that are sufficiently thin. The accuracy range was studied by Poggio and Adams (ref. 11) where an

extended thin-wire kernel was developed for wires that are too thick for the thin-wire approximation.

The derivation of the extended thin-wire kernel starts with the current on the surface of the source segment with surface density,

$$J(z') = I(z')/(2\pi a) ,$$

where a is the radius of the source segment. The geometry for evaluation of the fields is shown in figure 5. A current filament of strength $Id\phi/(2\pi)$ is integrated over ϕ with

$$\rho' = [\rho^2 + a^2 - 2a\rho \cos \phi]^{1/2} , \tag{80}$$

$$r = [\rho'^2 + (z-z')^2]^{1/2} . \tag{81}$$

Thus, the z component of the field of the current tube is

$$E_z^t(\rho,z) = \frac{1}{2\pi} \int_0^{2\pi} E_z^f(\rho',z)d\phi . \tag{82}$$

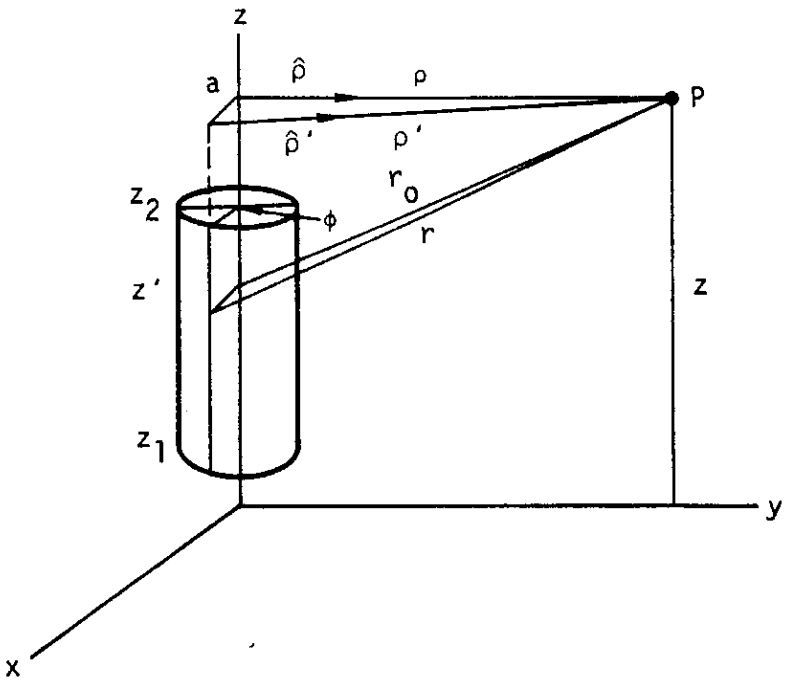

Figure 5. Current Geometry for the Extended Thin-Wire Kernel.

For the ρ component of field, the change in the direction of $\hat{\rho}'$ must be considered. The field in the direction $\hat{\rho}$ is

$$E_\rho^t(\rho,z) = \frac{1}{2\pi}\int_o^{2\pi} E_\rho^f(\rho',z)(\hat{\rho}\cdot\hat{\rho}')d\phi \ , \tag{83}$$

where

$$\hat{\rho}\cdot\hat{\rho}' = \frac{\rho - a\cos\phi}{\rho'} = \frac{\partial\rho'}{\partial\rho}$$

The integrals over ϕ in equations (82) and (83) cannot be evaluated in closed form. Poggio and Adams, however, have evaluated them as a series in powers of a^2 (ref. 11). The first term in the series gives the thin-wire kernel. For the extended thin-wire kernel, the second term involving a^2 is retained with terms of order a^4 neglected. As with the thin-wire kernel, the field observation point is on the segment surface. Hence, when evaluating the field on the source segment, $\rho = a$.

The field equations with the extended thin-wire approximation are given below. For a sinusoidal current of equation (70),

$$E_\rho(\rho,z) = \frac{-j\eta}{2k^2\lambda}\left[(z'-z)I\frac{\partial G_2}{\partial z'} + IG_2 - (z'-z)G_2\frac{\partial I}{\partial z'}\right]_{z_1}^{z_2} , \tag{84}$$

$$E_z(\rho,z) = \frac{j\eta}{2k^2\lambda}\left[G_1\frac{\partial I}{\partial z'} - I\frac{\partial G_1}{\partial z'}\right]_{z_1}^{z_2} , \tag{85}$$

For a constant current of strength I_o,

$$E_\rho(\rho,z) = \frac{I}{\lambda}\frac{j\eta}{2k^2}\left[\frac{\partial G_1}{\partial \rho}\right]_{z_1}^{z_2}, \tag{86}$$

$$E_z(\rho,z) = -\frac{I}{\lambda}\frac{j\eta}{2k^2}\left\{\left[\frac{\partial G_1}{\partial z'}\right]_{z_1}^{z_2} + k^2\left[1-\frac{(ka)^2}{4}\right]\int_{z_1}^{z_2} G_o\,dz' - \frac{(ka)^2}{4}\left[\frac{\partial G_o}{\partial z'}\right]_{z_1}^{z_2}\right\}. \tag{87}$$

The term G_1 is the series approximation of

$$G_1^t = \frac{1}{2\pi}\int_o^{2\pi} G\,d\phi, \tag{88}$$

where

$$G = \exp(-jkr)/r.$$

Neglecting terms of order a^4,

$$G_1 = G_o\left\{1 - \frac{a^2}{2r_o^2}(1+jkr_o) + \frac{a^2\rho^2}{4r_o^4}\left[3(1+jkr_o) - k^2r_o^2\right]\right\}, \tag{89}$$

$$\frac{\partial G_1}{\partial z'} = \frac{(z-z')}{r_o^2}G_o\left\{(1+jkr_o) - \frac{a^2}{2r_o^2}\left[3(1+jkr_o) - k^2r_o^2\right] - \frac{a^2\rho^2}{4r_o^4}\left[jk^3r_o^3 + 6k^2r_o^2 - 15(1+jkr_o)\right]\right\}, \tag{90}$$

$$\frac{\partial G_1}{\partial \rho} = -\frac{\rho G_o}{r_o^2}\left\{(1+jkr_o) - \frac{a^2}{r_o^2}\left[3(1+jkr_o) - k^2r_o^2\right]\right.$$

$$\left. - \frac{a^2\rho^2}{4r_o^4}\left[jk^3r_o^3 + 6k^2r_o^2 - 15(1+jkr_o)\right]\right\} . \tag{91}$$

The term G_2 is the series approximation of

$$G_2^t = \frac{1}{2\pi}\int_o^{2\pi} \frac{\rho - a\cos\phi}{\rho'^2} G\, d\phi . \tag{92}$$

To order a^2,

$$G_2 = \frac{G_o}{\rho}\left\{1 + \frac{a^2\rho^2}{4r_o^4}\left[3(1+jkr_o) - k^2r_o^2\right]\right\} , \tag{93}$$

$$\frac{\partial G_2}{\partial z'} = \frac{(z-z')}{\rho r_o^2} G_o \left\{(1+jkr_o) - \frac{a^2\rho^2}{4r_o^4}\left[jk^3r_o^3 + 6k^2r_o^2 - 15(1+jkr_o)\right]\right\} . \tag{94}$$

Equation (86) makes use of the relation

$$(\hat{\rho}\cdot\hat{\rho}')\frac{\partial G}{\partial \rho'} = \frac{\partial G}{\partial \rho'}\frac{\partial \rho'}{\partial \rho} = \frac{\partial G}{\partial \rho} , \tag{95}$$

while equation (87) follows from

$$G_1 = \left[1 - \frac{(ka)^2}{4} - \frac{a^2}{4}\frac{\partial^2}{\partial z'^2}\right] G_o . \tag{96}$$

When the observation point is within the wire ($\rho<a$), a series expansion in ρ rather than a is used for G_o and G_2. For G_1 this simply involves interchanging ρ and a in equations (89) and (90). Then for $\rho < a$, with

$$r_a = \left[a^2 + (z-z')^2\right]^{1/2} , \tag{97}$$

$$G_a = \exp(-jkr_a)/r_a \ , \tag{98}$$

the expressions for G_1, G_2 and their derivatives are

$$G_1 = G_a \left\{ 1 - \frac{\rho^2}{2r_a^2}(1+jkr_a) + \frac{a^2\rho^2}{4r_a^4}\left[3(1+jkr_a) - k^2r_a^2\right] \right\} \ , \tag{99}$$

$$\frac{\partial G_1}{\partial z'} = \frac{(z-z')}{r_a^2} G_a \left\{ (1+jkr_a) - \frac{\rho^2}{2r_a^2}\left[3(1+jkr_a) - k^2r_a^2\right] - \frac{a^2\rho^2}{4r_a^4}\left[jk^3r_a^3 + 6k^2r_a^2 - 15(1+jkr_a)\right] \right\} \ , \tag{100}$$

$$\frac{\partial G_1}{\partial \rho} = -\frac{\rho}{r_a^2} G_a \left\{ (1+jkr_a) - \frac{a^2}{2r_a^2}\left[3(1+jkr_a) - k^2r_a^2\right] \right\} \ , \tag{101}$$

$$G_2 = -\frac{\rho}{2r_a^2} G_a \ (1+jkr_a) \ , \tag{102}$$

$$\frac{\partial G_2}{\partial z'} = -\frac{(z-z')\rho}{2r_a^4} G_a \left[3(1+jkr_a) - k^2r_a^2\right] \ . \tag{103}$$

Special treatment of bends in wires is required when the extended thin-wire kernel is used. The problem stems from the cancellation of terms evaluated at z_1 and z_2 in the field equations when segments are part of a continuous wire. The current expansion in NEC results in a current having a continuous value and derivative along a wire without junctions. This ensures that for two adjacent segments on a straight wire, the contributions to the z component of electric field at z_2 of the first segment exactly cancel the contributions from z_1, representing the same point, for the second segment. For a straight wire of several segments, the only contributions to E_z with either the thin-wire or extended thin-wire kernel come from the two wire ends and the integral of G_o along the wire. For the ρ component of field or either component at a bend, while there is not complete cancellation, there may be partial cancellation of large end contributions.

The cancellation of end terms makes necessary a consistent treatment of the current on both sides of a bend for accurate evaluation of the field. This is easily accomplished with the thin-wire kernel since the current filament on the wire axis is physically continuous around a bend. However, the current tube assumed for the extended thin-wire kernel cannot be continuous around its complete circumference at a bend. This was found to reduce the solution accuracy when the extended thin-wire kernel was used for bent wires.

To avoid this problem in NEC, the thin-wire form of the end terms in equations (71) through (74) is always used at a bend or change in radius. The extended thin-wire kernel is used only at segment ends where two parallel segments join, or at free ends. The switch from extended thin-wire form to the thin-wire form is made from one end of a segment to the other rather than between segments where the cancellation of terms is critical.

When segments are separated by a large distance, the interaction may be computed with sufficient accuracy by treating the segment current as an infinitesimal current element at the segment center. In spherical coordinates, with the segment at the origin along the $\Theta = 0$ axis, the electric field is

$$E_r(r,\Theta) = \frac{M\eta}{2\pi r^2} \exp(-jkr)\left(1 - \frac{j}{kr}\right) \cos\Theta \ ,$$

$$E_\Theta(r,\Theta) = \frac{M\eta}{4\pi r^2} \exp(-jkr)\left(1+jkr - \frac{j}{kr}\right) \sin\Theta \ .$$

The dipole moment M for a constant current I on a segment of length Δ_i is

$$M = I\ \Delta_i \ .$$

For a current $I \cos[k(s - s_i)]$ with $|s - s_i| < \Delta_i/2$,

$$M = \frac{2I}{k} \sin(k\Delta_i/2) \ ,$$

while for a current $I \sin[k(s - s_i)]$,

$$M = 0 \ .$$

Use of this approximation saves a significant amount of time in evaluating the interaction matrix elements for large structures. The minimum interaction distance at which it is used is selected by the user in NEC. A default distance of one wavelength is set, however.

For each of the three methods of computing the field at a segment due to the current on another segment, the field is evaluated on the surface of the observation segment. Rather than choosing a fixed point on the segment surface, the field is evaluated at the cylindrical coordinates ρ', z with the source segment at the origin. If the center point on the axis of the observation segment is at ρ, z, then

$$\rho' = \left[\rho^2 + a_o^2\right]^{1/2} ,$$

where a_o is the radius of the observation segment. Also, the component of E_ρ tangent to the observation segment is computed as

$$\vec{E}_\rho \cdot \hat{s} = (\hat{\rho}\cdot\hat{s}) \frac{\rho}{\rho'} E_\rho .$$

Inclusion of the factor ρ/ρ', which is the cosine of the angle between $\hat{\rho}$ and $\hat{\rho}'$, is necessary for accurate results at bends in thick wires.

4. THE MATRIX EQUATION FOR CURRENT

For a structure having N_s wire segments and N_p patches, the order of the matrix in equation (19) is $N = N_s + 2N_p$. In NEC the wire segment equations occur first in the linear system so that, in terms of submatrices, the equation has the form

$$\begin{bmatrix} A & B \\ C & D \end{bmatrix} \begin{bmatrix} I_w \\ I_p \end{bmatrix} = \begin{bmatrix} E_w \\ H_p \end{bmatrix} ,$$

with equations derived from equation (14) in odd numbered rows in the lower set and equation (15) in even rows. I_w is then the column vector of segment

basis function amplitudes, and I_p is the patch-current amplitudes (J_{1j}, J_{2j}, $j=1,\ldots,N_p$). The elements of E_w are the left-hand side of equation (13) evaluated at segment centers, while H_p contains, alternately, the left-hand sides of equations (14) and (15) evaluated at patch centers.

A matrix element A_{ij} in submatrix A represents the electric field at the center of segment i due to the j^{th} segment basis function, centered on segment j. A matrix element D_{ij} in submatrix D represents a tangential magnetic field component at patch k due to a surface-current pulse on patch ℓ where

$$k = \text{Int}\left[(i-1)/2\right] + 1 \ ,$$

$$\ell = \text{Int}\left[(j-1)/2\right] + 1 \ ,$$

and Int[] indicates truncation. The source pulse is in the direction $\hat{t}_1$ when j is odd, and direction $\hat{t}_2$ when j is even. When $k = \ell$ the contribution of the surface integral is zero since the vector product is zero on the flat patch surface, although a ground image may produce a contribution. However, for $k = \ell$, there is a contribution of $\pm$ 1/2 from the coefficient of $\vec{J}_s(\vec{r})$ in equation (14) or (15). Matrix elements in submatrices B and C represent electric fields due to surface-current pulses and magnetic fields due to segment basis functions, respectively. These present no special problems since the source and observation points are always separated.

5. SOLUTION OF THE MATRIX EQUATION

The matrix equation,

$$[G]\ [I] = [E] \ , \tag{104}$$

is solved in NEC by Gauss elimination (ref. 19). The basic step is factorization of the matrix G into the product of an upper triangular matrix U and a lower triangle matrix L where

$$G = [L]\ [U] \ .$$

The matrix equation is then

$$[L]\ [U]\ [I] = [E] \ , \tag{105}$$

from which the solution, I, is computed in two steps as

$$[L]\,[F] = [E]\ , \tag{106}$$

and

$$[U]\,[I] = [F]\ . \tag{107}$$

Equation (106) is first solved for F by forward substitution, and equation (107) is then solved for I by backward substitution.

The major computational effort is factoring G into L and U. This takes approximately $1/3\ N^3$ multiplication steps for a matrix of order N compared to N^3 for inversion of G by the Gauss-Jordan method. Solution of equations (106) and (107), making use of the triangular properties of L and U, takes approximately as many multiplications as would be required for multiplication of G^{-1} by the column vector E. The factored matrices L and U are saved in NEC since the solution for induced current may be repeated for a number of different excitations. This, then, requires only the repeated solution of equations (106) and (107).

Computation of the elements of the matrix G and solution of the matrix equation are the two most time-consuming steps in computing the response of a structure, often accounting for over 90% of the computation time. This may be reduced substantially by making use of symmetries of the structure, either symmetry about a plane, or symmetry under rotation.

In rotational symmetry, a structure having M sectors is unchanged when rotated by any multiple of 360/M degrees. If the equations for all segments and patches in the first sector are numbered first and followed by successive sectors in the same order, the matrix equation can be expanded in submatrices in the form

$$\begin{bmatrix} A_1 & A_2 & A_3 & \cdots & A_{M-1} & A_M \\ A_M & A_1 & A_2 & \cdots & A_{M-2} & A_{M-1} \\ A_{M-1} & A_M & A_1 & & A_{M-3} & A_{M-2} \\ \vdots & & & & \vdots & \vdots \\ A_2 & A_3 & A_4 & & A_M & A_1 \end{bmatrix} \begin{bmatrix} I_1 \\ I_2 \\ I_3 \\ \vdots \\ I_M \end{bmatrix} = \begin{bmatrix} E_1 \\ E_2 \\ E_3 \\ \vdots \\ E_M \end{bmatrix} \tag{108}$$

If there are N_c equations in each sector, E_i and I_i are N_c element column vectors of the excitations and currents in sector i. A_i is a submatrix of order N_c containing the interaction fields in sector 1 due to currents in sector i. Due to symmetry, this is the same as the fields in sector k due to currents in sector i + k, resulting in the repetition pattern shown. Thus only matrix elements in the first row of submatrices need be computed, reducing the time to fill the matrix by a factor of 1/M.

The time to solve the matrix equation can also be reduced by expanding the excitation subvectors in a discrete Fourier series as

$$E_i = \sum_{k=1}^{M} S_{ik} E_k \qquad i=1,\ldots,M \ , \tag{109}$$

$$E_i = \frac{1}{M} \sum_{k=1}^{M} S^*_{ik} E_k \qquad i=1,\ldots,M \ , \tag{110}$$

where

$$S_{ik} = \exp\left[j2\pi(i-1)(k-1)/M\right] \ , \tag{111}$$

$j=\sqrt{-1}$, and * indicates the conjugate of the complex number. Examining a component in the expansion,

$$E = \begin{bmatrix} S_{1k} E_k \\ S_{2k} E_k \\ \cdot \\ \cdot \\ \cdot \\ S_{Mk} E_k \end{bmatrix} \ , \tag{112}$$

it is seen that the excitation differs from sector to sector only by a uniform phase shift. This excitation of a rotationally symmetric structure results in a solution having the same form as the excitation, i.e.,

$$I = \begin{bmatrix} S_{1k}\ I_k \\ S_{2k}\ I_k \\ . \\ . \\ . \\ S_{Mk}\ I_k \end{bmatrix} \tag{113}$$

It can be shown that this relation between solution and excitation holds for any matrix having the form of that in equation (108). Substituting these components of E and I into equation (108) yields the following matrix equation of order N_c relating I_k to E_k:

$$\left[S_{1k}\ A_1 + S_{2k}\ A_2 + \ldots + S_{Mk}\ A_M\right]\ \left[I_k\right] = S_{1k}\ \left[E_k\right] \quad . \tag{114}$$

The solution for the total excitation is then obtained by an inverse transformation,

$$I_i = \sum_{k=1}^{M} S_{ik}\ I_k \qquad i=1, \ldots, M \ . \tag{115}$$

The solution procedure, then, is first to compute the M submatrices A_i and Fourier-transform these to obtain

$$A_i = \sum_{k=1}^{M} S_{ik}\ A_k \qquad i=1, \ldots, M \ . \tag{116}$$

The matrices A_i, of order N_c, are then each factored into upper and lower triangular matrices by the Gauss elimination method. For each excitation vector, the transformed subvectors are then computed by equation (110) and the transformed current subvectors are obtained by solving the M equations,

$$[A_i]\ [I_i] = [E_i] \ . \tag{117}$$

The total solution is then given by equation (115).

The same procedure can be used for structures that have planes of symmetry. The Fourier transform is then replaced by even and odd excitations about each symmetry plane. All equations remain the same with the exception

that the matrix S with elements S_{ij}, given by equation (111), is replaced by the following matrices:

For one plane of symmetry,

$$S = \begin{bmatrix} 1 & 1 \\ 1 & -1 \end{bmatrix};$$

For two orthogonal planes of symmetry,

$$S = \begin{bmatrix} 1 & 1 & 1 & 1 \\ 1 & -1 & 1 & -1 \\ 1 & 1 & -1 & -1 \\ 1 & -1 & -1 & 1 \end{bmatrix};$$

and for three orthogonal symmetry planes,

$$S = \begin{bmatrix} 1 & 1 & 1 & 1 & 1 & 1 & 1 & 1 \\ 1 & -1 & 1 & -1 & 1 & -1 & 1 & -1 \\ 1 & 1 & -1 & -1 & 1 & 1 & -1 & -1 \\ 1 & -1 & -1 & 1 & 1 & -1 & -1 & 1 \\ 1 & 1 & 1 & 1 & -1 & -1 & -1 & -1 \\ 1 & -1 & 1 & -1 & -1 & 1 & -1 & 1 \\ 1 & 1 & -1 & -1 & -1 & -1 & 1 & 1 \\ 1 & -1 & -1 & 1 & -1 & 1 & 1 & -1 \end{bmatrix}.$$

For either rotational or plane symmetry, the procedure requires factoring of M matrices of order N_c rather than one matrix of order MN_c. Each excitation then requires the solution of the M matrix equations. Since the time for factoring is approximately proportional to the cube of the matrix order and the time for solution is proportional to the square of the order, the symmetry results in a reduction of factor time by M^{-2} and in solution time by M^{-1}. The time to compute the transforms is generally small compared to the time for matrix operations since it is proportional to a lower power of N_c. Symmetry also reduces the number of locations required for matrix storage by M^{-1} since only the first row of submatrices need be stored. The transformed matrices, A_i, can replace the matrices A_i as they are computed.

NEC includes a provision to generate and factor an interaction matrix and save the result on a file. A later run, using the file, may add to the structure and solve the complete model without unnecessary repetition of calculations. This procedure is called the Numerical Green's Function (NGF) option since the effect is as if the free space Green's function in NEC were replaced by the Green's function for the structure on the file. The NGF is particularly useful for a large structure, such as a ship, on which various antennas will be added or modified. It also permits taking advantage of partial symmetry since a NGF file may be written for the symmetric part of a structure, taking advantage of the symmetry to reduce computation time. Unsymmetric parts can then be added in a later run.

For the NGF solution the matrix is partitioned as

$$\begin{bmatrix} A & B \\ C & D \end{bmatrix} \begin{bmatrix} I_1 \\ I_2 \end{bmatrix} = \begin{bmatrix} E_1 \\ E_2 \end{bmatrix} ,$$

where A is the interaction matrix for the initial structure, D is the matrix for the added structure, and B and C represent mutual interactions. The current is computed as

$$I_2 = \left[D - CA^{-1}B\right]^{-1} \left[E_2 - CA^{-1} E_1\right] ,$$

$$I_1 = A^{-1} E_1 - A^{-1} BI_2 ,$$

after the factored matrix A has been read from the NGF file along with other necessary data.

Electrical connections between the new structure and the old (NGF) structure require special treatment. If a new wire or patch connects to an old wire the current basis function for the old wire segment is changed by the modified condition at the junction. The old basis function is given zero amplitude by adding a new equation having all zeros except for a one in the column of the old basis function. A new column is added for the corrected basis function. When a new wire connects to an old patch the patch must be divided into four new patches to apply the connection condition of equation (51). Hence both the current basis function and match point for the old patch are replaced.

Section IV
Effect of a Ground Plane

In the integral equation formulation used in NEC, a ground plane changes the solution in three ways: (1) by modifying the current distribution through near-field interaction; (2) by changing the field illuminating the structure; and (3) by changing the reradiated field. Effects (2) and (3) are easily analyzed by plane-wave reflection as a direct ray and a ray reflected from the ground. The reradiated field is not a plane wave when it reflects from the ground, but, as can be seen from reciprocity, plane-wave reflection gives the correct far-zone field. Analysis of the near-field interaction effect is, however, much more difficult.

In Section II, the kernels of the integral equations are free-space Green's functions, representing the E or H field at a point $\vec{r}$ due to an infinitesimal electric current element at $\vec{r}'$. When a ground is present the free space Green's functions must be replaced by Green's functions for the ground problem. The solution for the fields of current elements in the presence of a ground plane was developed by Arnold Sommerfeld (ref. 20). While this solution has been used directly in integral-equation computer codes, excessive computation time greatly limits its use. Numerous approximations to the Sommerfeld solution have been developed that require less time for evaluation but all have limited applicability.

The NEC code has three options for grounds. The most accurate for lossy grounds uses the Sommerfeld solution for interaction distances less than one wavelength and an asymptotic expansion for larger distances. To keep the solution time reasonable, a grid of values of the Sommerfeld solution is generated and interpolation is used to find specific values. This method is presently implemented only for wires in NEC but could be extended to patches. The solution for a perfectly conducting ground is much simpler since the ground may be replaced by the image of the currents above it. The third option models a lossy ground by a modified image method using the Fresnel plane-wave reflection coefficients. While specular reflection does not accurately describe the behavior of near fields, the approximation has been found to provide useful results for structures that are not too near to the ground (refs. 21, 22). The attraction of this method is its simplicity and speed of computation which are the same as for the image method for perfect ground.

1. THE SOMMERFELD/NORTON METHOD

The Sommerfeld/Norton ground option in NEC originated with the code WFLLL2A (ref. 23) which uses numerical evaluation of the Sommerfeld integrals for ground fields when the interaction distance is small and uses Norton's asymptotic approximations (ref. 24) for larger distances. Since evaluation of the Sommerfeld integrals is very time consuming, a code, SOMINT, was developed (ref. 25) which uses bivariate interpolation in a table of pre-computed Sommerfeld integral values to obtain the field values needed for integration over current distributions. This method greatly reduces the required computation time. NEC uses a similar interpolation method with modifications to allow wires closer to the air-ground interface and to further reduce computation time. Although the code WFLLL2A allows wires both above and below the interface, both NEC and SOMINT are presently restricted to wires on the free-space side. The method used in NEC to evaluate the field over ground is described below, and the numerical evaluation of the Sommerfeld integrals to fill the interpolation grid is discussed in Section IV-2.

The electric field above an air-ground interface due to an infinitesimal current element of strength $I\ell$ also above the interface, with parameters shown in figure 6, is given by the following expressions:

$$E_\rho^V = C_1 \frac{\partial^2}{\partial\rho\partial z}\left[G_{22} - G_{21} + k_1^2 V_{22}\right] , \tag{118}$$

$$E_z^V = C_1\left(\frac{\partial^2}{\partial z^2} + k_2^2\right)\left(G_{22} - G_{21} + k_1^2 V_{22}\right) , \tag{119}$$

$$E_\rho^H = C_1 \cos\phi\left[\frac{\partial^2}{\partial\rho^2}\left(G_{22} - G_{21} + k_2^2 V_{22}\right) + k_2^2\left(G_{22} - G_{21} + U_{22}\right)\right] , \tag{120}$$

$$E_\phi^H = -C_1 \sin\phi\left[\frac{1}{\rho}\frac{\partial}{\partial\rho}\left(G_{22} - G_{21} + k_2^2 V_{22}\right) + k_2^2\left(G_{22} - G_{21} + U_{22}\right)\right] , \tag{121}$$

$$E_z^H = C_1 \cos\phi \frac{\partial^2}{\partial z\partial\rho}\left(G_{22} + G_{21} - k_1^2 V_{22}\right) , \tag{122}$$

$$C_1 = \frac{-j\omega I\ell\mu_o}{4\pi k_2^2} , \tag{123}$$

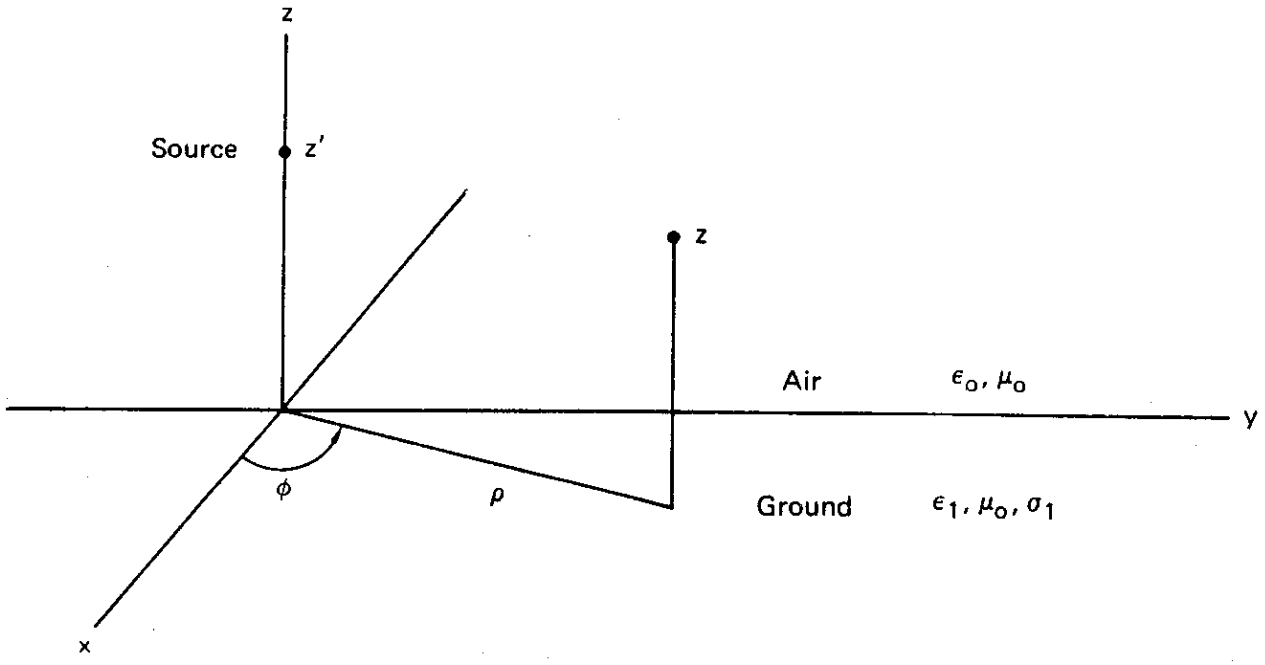

Figure 6. Coordinates for Evaluating the Field of a Current Element Over Ground.

$$k_1^2 = \omega^2 \mu_o \varepsilon_o \left(\frac{\varepsilon_1}{\varepsilon_o} - \frac{j\sigma_1}{\omega \varepsilon_o} \right) , \tag{124}$$

$$k_2^2 = \omega^2 \mu_o \varepsilon_o , \tag{125}$$

where the superscript indicates a vertical (V) or horizontal (H) current element and the subscript indicates the cylindrical component of the field vector. The horizontal current element is along the x axis.

G_{22} and G_{21} are the free space and image Green's functions

$$G_{22} = \exp(-jk_2 R_2)/R_2 , \tag{126}$$

$$G_{21} = \exp(-jk_2 R_1)/R_1 , \tag{127}$$

where

$$R_1 = \left[\rho^2 + (z + z')^2 \right]^{1/2} , \tag{128}$$

$$R_2 = \left[\rho^2 + (z - z')^2 \right]^{1/2} , \tag{129}$$

and U_{22} and V_{22} are Sommerfeld integrals involving the zeroth order Bessel function, J_o

$$U_{22} = 2\int_o^\infty \frac{\exp[-\gamma_2(z + z')]\ J_o(\lambda\rho)\lambda d\lambda}{\gamma_1 + \gamma_2} \quad , \tag{130}$$

$$V_{22} = 2\int_o^\infty \frac{\exp[-\gamma_2(z + z')]\ J_o(\lambda\rho)\lambda d\lambda}{k_1^2\,\gamma_2 + k_2^2\,\gamma_1} \quad , \tag{131}$$

where

$$\gamma_1 = \left(\lambda^2 - k_1^2\right)^{1/2} \quad , \tag{132}$$

$$\gamma_2 = \left(\lambda^2 - k_2^2\right)^{1/2} \quad . \tag{133}$$

In NEC we need to compute the fields due to current filaments with arbitrary length and orientation by combining the field components in equations (118) through (122) and integrating over current distributions composed of constant, sine, and cosine components. Direct numerical integration over the segments is difficult due to singularities in the fields. G_{22} has a $1/R_2$ singularity while G_{21}, U_{22} and V_{22} each have $1/R_1$ singularities. The derivatives in the field expressions result in $1/R_3$ singularities with a triplet-like behavior in the field components parallel to the current filament. The resulting cancellation makes accurate numerical integration near the singularity very difficult.

The free-space field has a similar singularity, but as discussed in Section III-3, the integral over a straight filament may be evaluated in closed form for a sinusoidal current with free-space wavelength and involves only a numerical integration of G_{22} for a constant current. The dominant singular component of the ground field may be integrated in the same way. The terms involving G_{22} in equation (118) through (122) are, in fact, the field of the current element in free space, and their integral is obtained from the free-space routines in NEC.

The remaining terms represent the field due to ground and are singular at $R_1 = 0$. The singularities in U_{22} and V_{22} result from the failure of the integrals in equations (130) and (131) to converge without the exponential and

Bessel functions as ρ and $z + z'$ go to zero. The singular behavior of U_{22} and V_{22} as ρ and $z + z'$ go to zero may be found by setting $\gamma_1 = \gamma_2 = \lambda$ since the dominant contributions to the integrals for small ρ and $z + z'$ come from λ much greater than k_1 or k_2. Here, however, we only replace γ_1 by γ_2 and use the integrals

$$V_{22} \approx 2\int_o^\infty \frac{\exp[-\gamma_2(z + z')]\ J_o(\lambda\rho)\lambda d\lambda}{\gamma_2(k_1^2 + k_2^2)} = \frac{2G_{21}}{k_1^2 + k_2^2} \quad , \tag{134}$$

$$U_{22} \approx \int_o^\infty \frac{\exp[-\gamma_2(z + z')]\ J_o(\lambda\rho)\lambda d\lambda}{\gamma_2} = G_{21} \tag{135}$$

$$|k_1|\rho << 1, \quad |k_1|(z + z') << 1,$$

which have the correct singular behavior and can be combined with the G_{21} terms. The field components due to ground [equation (108) through (122) without the G_{22} terms] may then be written as

$$G_\rho^V = C_1 \frac{\partial^2}{\partial\rho\partial z} k_1^2 V'_{22} + C_1 \frac{k_1^2 - k_2^2}{k_1^2 + k_2^2} \frac{\partial^2}{\partial\rho\partial z} G_{21} \quad , \tag{136}$$

$$G_z^V = C_1\left(\frac{\partial^2}{\partial z^2} + k_2^2\right) k_1^2 V'_{22} + C_1 \frac{k_1^2 - k_2^2}{k_1^2 + k_2^2}\left(\frac{\partial^2}{\partial z^2} + k_2^2\right) G_{21} \tag{137}$$

$$G_\rho^H = C_1 \cos\phi \left(\frac{\partial^2}{\partial\rho^2} k_2^2 V'_{22} + k_2^2 U'_{22}\right) - C_1 \cos\phi \frac{k_1^2 - k_2^2}{k_1^2 + k_2^2}\left(\frac{\partial^2}{\partial\rho^2} + k_2^2\right) G_{21} \quad , \tag{138}$$

$$G_\phi^H = -C_1 \sin\phi \left(\frac{1}{\rho}\frac{\partial}{\partial\rho} k_2^2 V'_{22} + k_2^2 U'_{22}\right) + C_1 \sin\phi \frac{k_1^2 - k_2^2}{k_1^2 + k_2^2}\left(\frac{1}{\rho}\frac{\partial}{\partial\rho} + k_2^2\right) G_{21} \quad , \tag{139}$$

$$G_z^H = -\cos\phi \; G_\rho^V \; , \tag{140}$$

where

$$U'_{22} = U_{22} - \frac{2k_2^2}{k_2^2 + k_1^2} \; G_{21} \; ,$$

$$= 2\int_o^\infty \left[\frac{1}{\gamma_1 + \gamma_2} - \frac{k_2^2}{\gamma_2(k_1^2 + k_2^2)}\right] \exp[-\gamma_2(z + z')] \tag{141}$$

$$\times \; J_o(\lambda\rho)\lambda d\lambda \quad ,$$

$$V'_{22} = V_{22} - \frac{2}{k_1^2 + k_2^2} \; G_{21} \; ,$$

$$= 2\int_o^\infty \left[\frac{1}{k_1^2 \; \gamma_2 + k_2^2 \; \gamma_1} - \frac{1}{\gamma_2 \; k_1^2 + k_2^2}\right] \tag{142}$$

$$\times \; \exp[-\gamma_2(z + z')] \; J_o(\lambda\rho)\lambda d\lambda \quad .$$

In equations (136) through (140) the dominant singular component has been subtracted out of V_{22} and combined with G_{21}. The integral for V'_{22} converges without the exponential or Bessel function factors and remains finite as ρ and $z + z'$ go to zero. The derivatives of V'_{22} in the field expressions have $1/R_1$ singularities, but this is much less of a problem for numerical integration than the previous $1/R_1^3$ singularity. The singularity could be taken out of U_{22} also, but, instead, a term is taken out that results in the final terms in equations (136) through (139) being the image field multiplied by $(k_1^2 - k_2^2)/(k_1^2 + k_2^2)$. The integral over the current filament of these image terms is evaluated by the free-space equations leaving only the U'_{22} and V'_{22} terms to be integrated numerically. U'_{22} still has a $1/R_1$ singularity, but that is no worse than the derivatives of V'_{22}. With the thin-wire approximation, R_1 is never less than the wire radius so the integration is not difficult in practical cases.

The components left for numerical integration over the current distribution are then

$$F_\rho^V = C_1 \frac{\partial^2}{\partial\rho\partial z} k_1^2 V'_{22} , \tag{143}$$

$$F_z^V = C_1\left(\frac{\partial^2}{\partial z^2} + k_2^2\right) k_1^2 V'_{22} , \tag{144}$$

$$F_\rho^H = C_1\cos\phi\left(\frac{\partial^2}{\partial\rho^2} k_2^2 V'_{22} + k_2^2 U'_{22}\right) , \tag{145}$$

$$F_\phi^H = -C_1\sin\phi\left(\frac{1}{\rho}\frac{\partial}{\partial\rho} k_2^2 V'_{22} + k_2^2 U'_{22}\right) , \tag{146}$$

$$F_z^H = -\cos\phi\ F_\rho^V . \tag{147}$$

Since the integrals in equations (141) and (142) cannot be evaluated in closed form the following terms must be evaluated by numerical integration over λ:

$$\frac{\partial^2 V'_{22}}{\partial\rho^2} = \int_o^\infty D_2 \exp\left[-\gamma_2(z + z')\right] J''_o(\lambda\rho)\lambda^3 d\lambda , \tag{148}$$

$$\frac{\partial^2 V'_{22}}{\partial z^2} = \int_o^\infty D_2 \gamma_2^2 \exp\left[-\gamma_2(z + z')\right] J_o(\lambda\rho)\lambda d\lambda , \tag{149}$$

$$\frac{\partial^2 V'_{22}}{\partial\rho\partial z} = -\int_o^\infty D_2\gamma_2 \exp\left[-\gamma_2(z + z')\right] J'_o(\lambda\rho)\lambda^2 d\lambda , \tag{150}$$

$$\frac{1}{\rho}\frac{\partial V'_{22}}{\partial\rho} = \frac{1}{\rho}\int_o^\infty D_2 \exp\left[-\gamma_2(z + z')\right] J'_o(\lambda\rho)\lambda^2 d\lambda , \tag{151}$$

$$V'_{22} = \int_o^\infty D_2 \exp\left[-\gamma_2(z + z')\right] J_o(\lambda\rho)\lambda d\lambda , \tag{152}$$

$$U'_{22} = \int_o^\infty D_1 \exp\left[-\gamma_2(z + z')\right] J_o(\lambda\rho)\lambda d\lambda , \tag{153}$$

where

$$D_1 = \frac{2}{\gamma_2 + \gamma_2} - \frac{2\,k_2^2}{\gamma_2(k_1^2 + k_2^2)} \quad , \tag{154}$$

$$D_2 = \frac{2}{k_1^2\,\gamma_2 + k_2^2\,\gamma_1} - \frac{2}{\gamma_2(k_1^2 + k_2^2)} \quad . \tag{155}$$

Evaluating these integrals over λ for each point needed in the numerical integration over the current distribution is slow on even the fastest computers. Hence an interpolation technique is used for the remaining field components as was done in the code SOMINT for the total field due to ground. Since the integrals depend only on ρ and $z + z'$ a grid of values is generated for the field components of equations (143) through (146) and bivariate interpolation is used to obtain values for integration over a current distribution.

To facilitate interpolation in the region of the $1/R_1$ singularity, the components are divided by a function having a similar singularity and interpolation is performed on the ratio. The field components of equations (143) through (146) are divided by $\exp(-jkR_1)/R_1$ for all values of R_1 to remove the singularity and the free-space phase factor before interpolation. The factors $\sin\phi$ or $\cos\phi$ are also omitted until after interpolation to avoid introducing the ϕ dependence. The surfaces to which interpolation is applied are then

$$I_\rho^V = C_1\,R_1\,\exp(jkR_1)\,\frac{\partial^2}{\partial\rho\partial z}\,k_1^2\,V_{22}' \quad , \tag{156}$$

$$I_z^V = C_1\,R_1\,\exp(jkR_1)\left(\frac{\partial^2}{\partial z^2} + k_2^2\right)k_1^2\,V_{22}' \quad , \tag{157}$$

$$I_\rho^H = C_1\,R_1\,\exp(jkR_1)\left(\frac{\partial^2}{\partial\rho^2}\,k_2^2\,V_{22}' + k_2^2\,U_{22}'\right) \quad , \tag{158}$$

$$I_\phi^H = -\,C_1\,R_1\,\exp(jkR_1)\left(\frac{1}{\rho}\,\frac{\partial}{\partial\rho}\,k_2^2\,V_{22}' + k_2^2\,U_{22}'\right) \quad . \tag{159}$$

After interpolation on the smoothed surfaces the results are multiplied by the omitted factors to give the correct values.

With the singularity removed, interpolation may be used for arbitrarily small values of ρ and $z + z'$. The values for $R_1 = 0$ in the interpolation grid must be found as limits for R_1 approaching zero, however, since the integrals

do not converge in this case. When ρ and $z + z'$ approach zero the dominant contributions in equations (148) through (153) come from large λ. Hence the singular behavior can be found by setting γ_1 and γ_2 equal to λ. First, however, it is necessary to approximate D_1 and D_2 for $|\lambda| >> |k_1|$ as

$$D_1 = C_2/\lambda \ , \ C_2 = \frac{k_1^2 - k_2^2}{k_1^2 + k_2^2} \ , \tag{160}$$

$$D_2 = C_3/\lambda^3, \ C_3 = \frac{k_2^2\left(k_1^2 - k_2^2\right)}{\left(k_1^2 + k_2^2\right)^2} \ . \tag{161}$$

For $|k_1|\rho << 1$ and $|k_1|(z + z') << 1$ the integrals become

$$\frac{\partial^2 V'_{22}}{\partial \rho^2} \approx C_3 \int_o^\infty \exp\left[-\lambda(z + z')\right] J''_o(\lambda\rho) \, d\lambda \ ,$$

$$= C_3\left[\frac{1 - \sin\theta}{\cos^2\theta} - 1\right] \frac{1}{R_1} \ , \tag{162}$$

$$\frac{\partial^2 V'_{22}}{\partial z^2} \approx C_3 \int_o^\infty \exp\left[-\lambda(z + z')\right] J_o(\lambda\rho) d\lambda = \frac{C_3}{R_1} \ , \tag{163}$$

$$\frac{\partial^2 V'_{22}}{\partial \rho \partial z} \approx - C_3 \int_o^\infty \exp\left[-\lambda(z + z')\right] J'_o(\lambda\rho) d\lambda = \frac{C_3(1 - \sin\theta)}{R_1 \cos\theta} \ , \tag{164}$$

$$\frac{1}{\rho} \frac{V'_{22}}{\partial \rho} \approx \frac{C_3}{\rho} \int_o^\infty \exp\left[-\lambda(z + z')\right] J'_o(\lambda\rho) \frac{1}{\lambda} d\lambda = \frac{-C_3(1 - \sin\theta)}{R_1 \cos^2\theta} \ , \tag{165}$$

$$U'_{22} \approx C_2 \int_o^\infty \exp\left[-\lambda(z + z')\right] J_o(\lambda\rho) \, d\lambda = \frac{C_2}{R_1} \ , \tag{166}$$

where

$$R_1 = \left[\rho^2 + (z + z')^2\right]^{1/2} \ , \tag{167}$$

$$\theta = \tan^{-1}\left[(z + z')/\rho\right] \ . \tag{168}$$

V'_{22} remains finite as R_1 goes to zero and hence is neglected. Equations (156) through (159) for R_1 approaching zero are then

$$I_\rho^V = C_1 C_3 k_1^2 \left(\frac{1 - \sin\theta}{\cos\theta}\right) , \tag{169}$$

$$I_z^V = C_1 C_3 k_1^2 , \tag{170}$$

$$I_\rho^H = C_1 k_2^2 \left[C_2 - C_3 + C_3\left(\frac{1 - \sin\theta}{\cos^2\theta}\right)\right] , \tag{171}$$

$$I_\phi^H = -C_1 k_2^2 \left[C_2 - C_3\left(\frac{1 - \sin\theta}{\cos^2\theta}\right)\right] . \tag{172}$$

Since the limiting values as R_1 goes to zero are functions of θ it is necessary to use R_1 and θ as the interpolation variables rather than ρ and $z + z'$.

Figures 7 through 10 are plots of the surfaces to which interpolation is applied for typical ground parameters. The width of the region of relatively rapid variation along the R_1 axis appears to be proportional to the wavelength

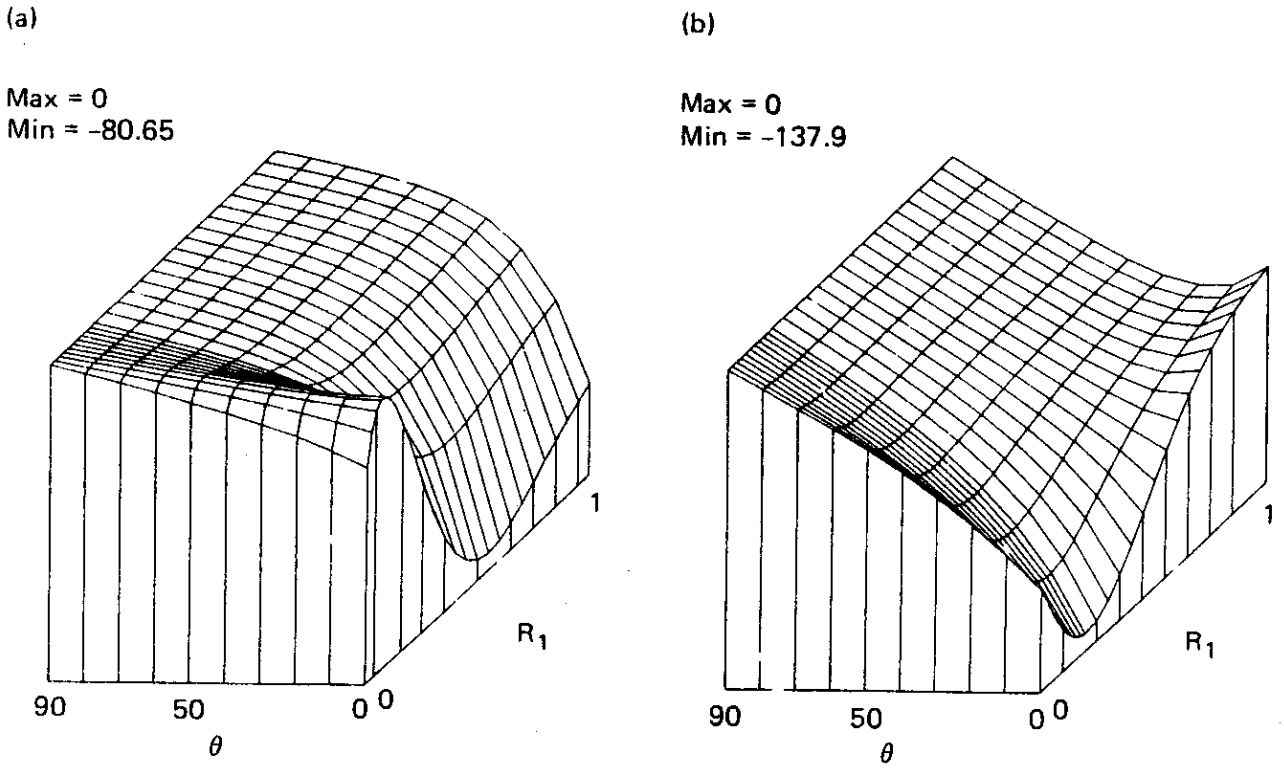

Figure 7. Real (a) and Imaginary (b) Parts of I_ρ^V for $\varepsilon_1/\varepsilon_o = 4$, $\sigma_1 = 0.001$ mhos/m, frequency = 10 MHz.

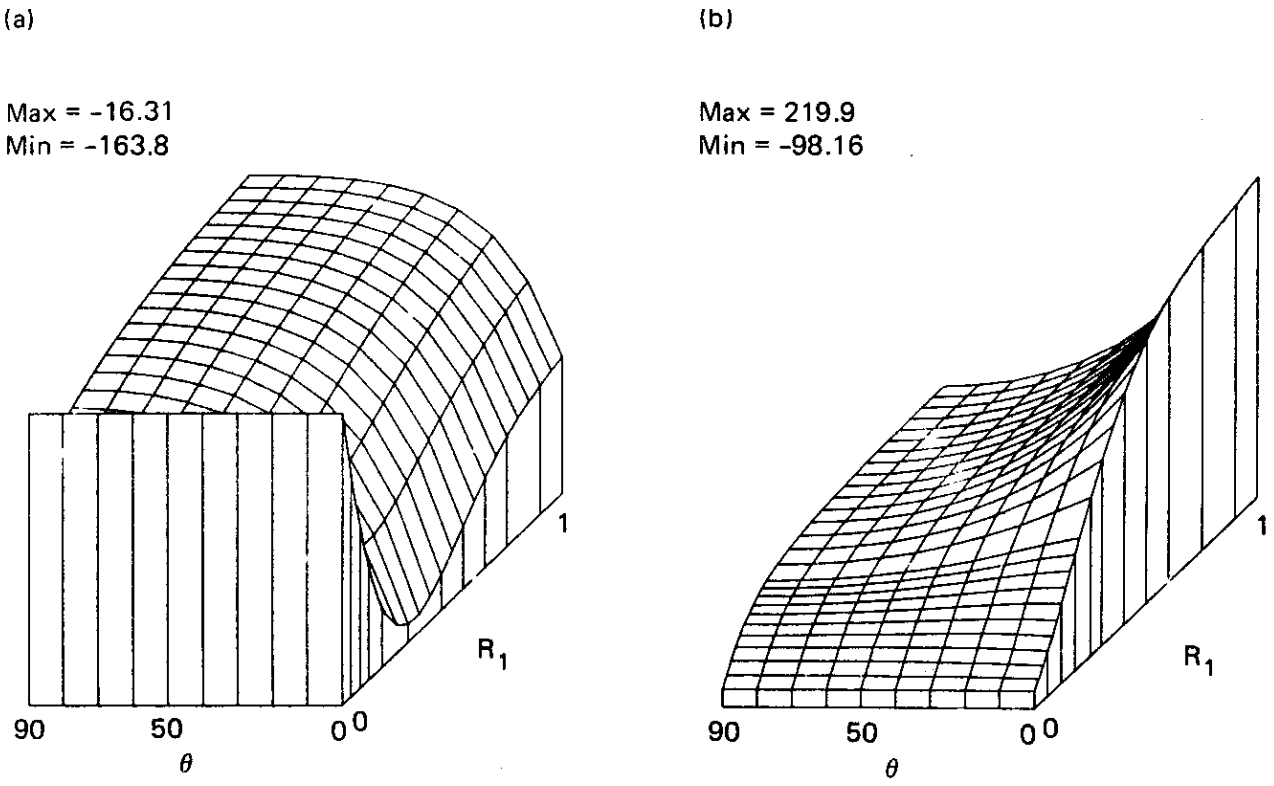

Figure 8. Real (a) and Imaginary (b) Parts of I_z^V for $\varepsilon_1/\varepsilon_o = 4$, $\sigma_1 = 0.001$ mhos/m, frequency = 10 MHz.

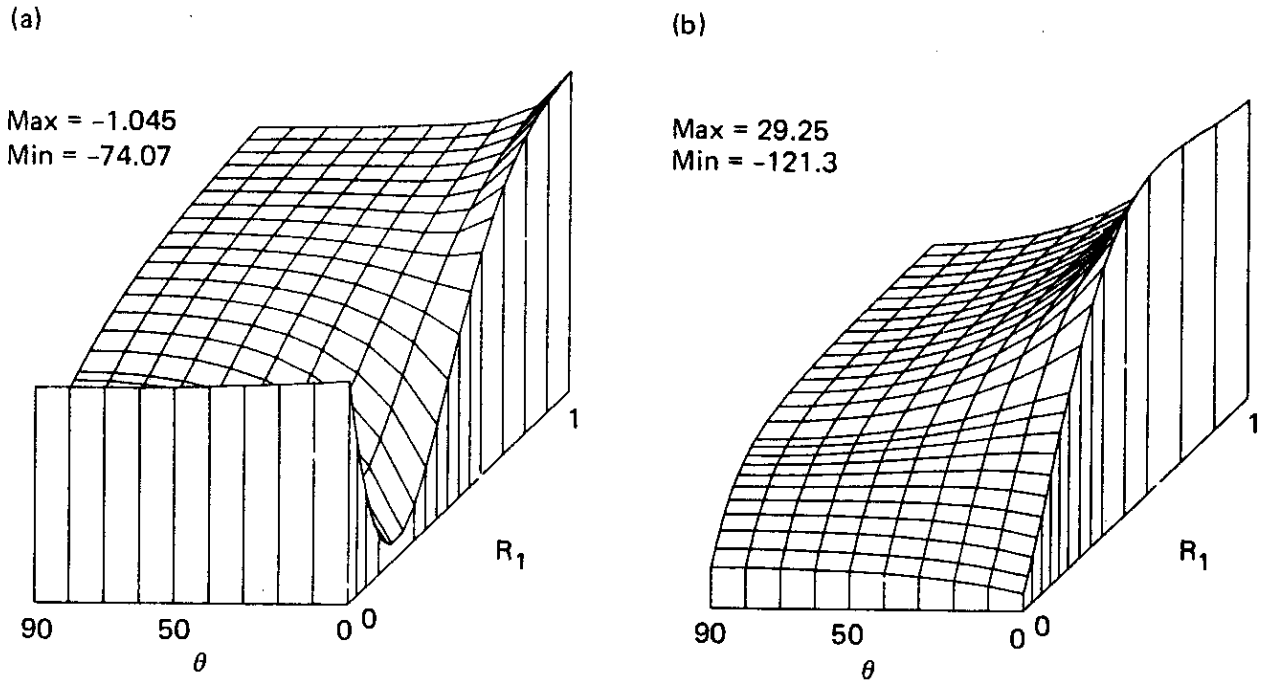

Figure 9. Real (a) and Imaginary (b) Parts of I_ρ^H for $\varepsilon_1/\varepsilon_o = 4$, $\sigma_1 = 0.001$ mhos/m, frequency = 10 MHz.

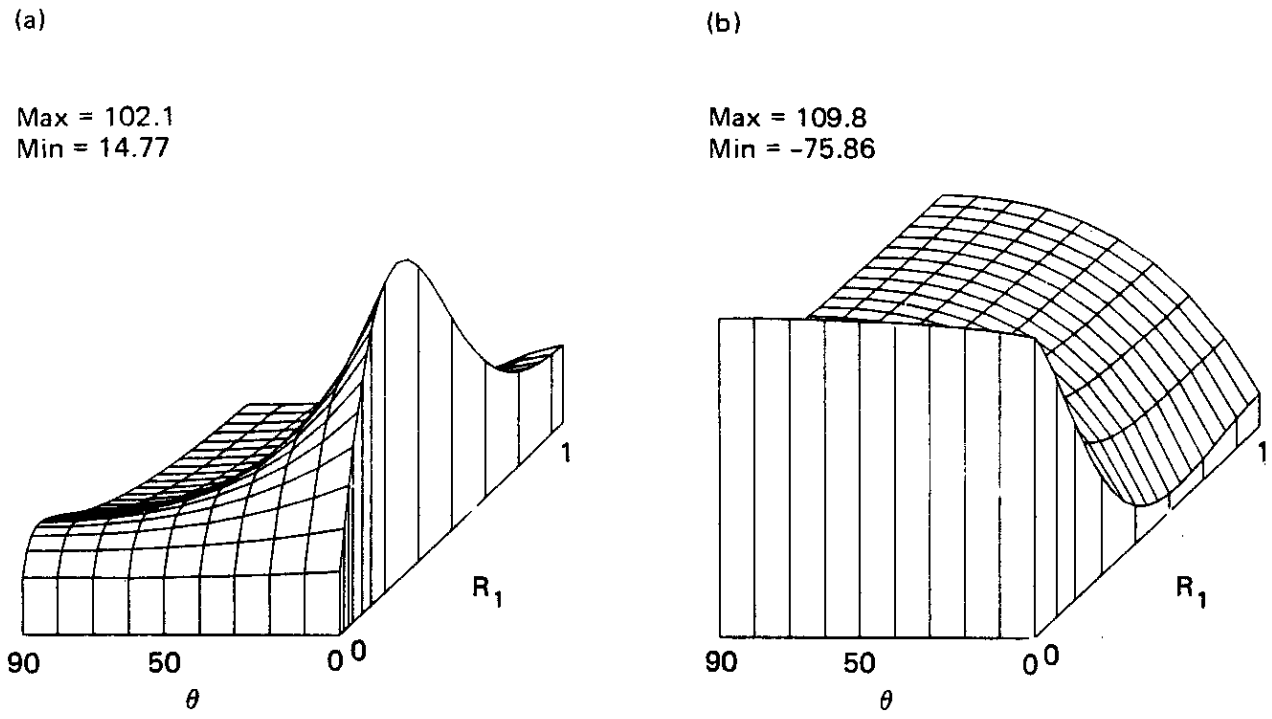

Figure 10. Real (a) and Imaginary (b) Parts of I_{ϕ}^{H} for $\varepsilon_1/\varepsilon_o = 4$, $\sigma_1 = 0.001$ mhos/m, frequency = 10 MHz.

in the lower medium and hence is concentrated closer to $R_1 = 0$ for larger dielectric constants. At a finite R_1, the functions approach zero as ε_1 and σ_1 become large. When loss is small the strong wave in the lower medium results in a significant evanescent wave along the interface in the upper medium as shown in figure 11.

In NEC the interpolation region from 0 to 1 wavelength in R_1 is divided into three grids, as shown in figure 12, on which bivariate cubic interpolation is used. For a given point, the correct grid region is determined and cubic surfaces in R_1 and θ, fit to a 4-point by 4-point region containing the desired point, are evaluated for each of the four quantities I_{ρ}^{V}, I_{z}^{V}, I_{ρ}^{H}, and I_{ϕ}^{H}. The grid point spacings used are:

Grid	ΔR_1	$\Delta\theta$
1	0.02λ	10°
2	0.05λ	5°
3	0.1λ	10°

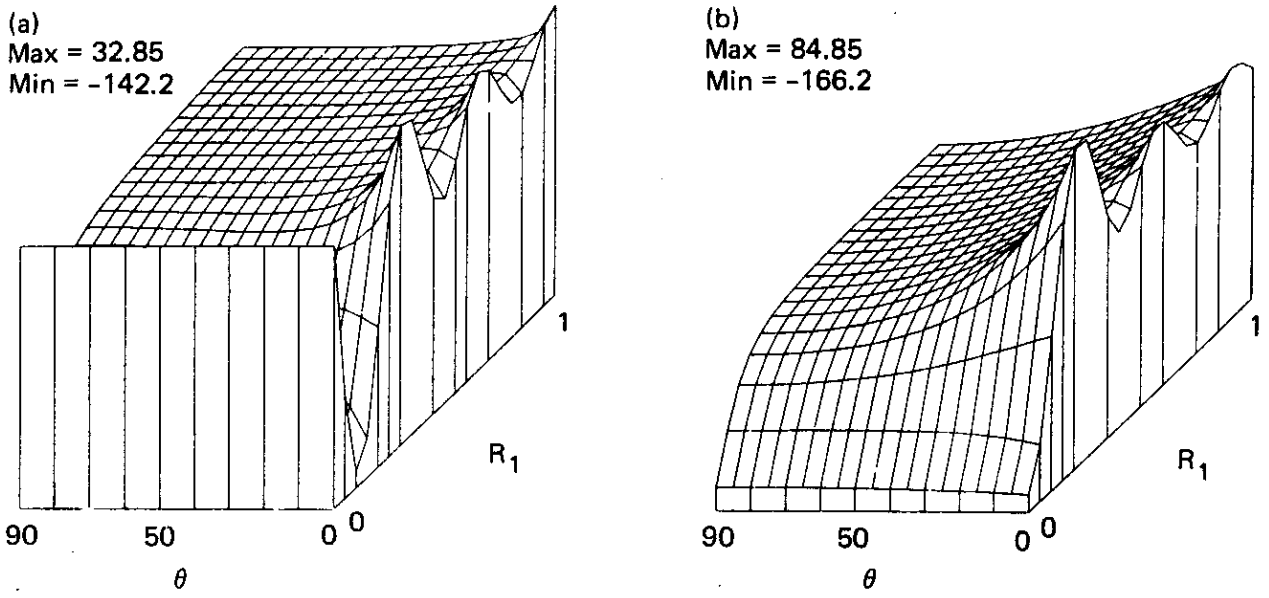

Figure 11. Real (a) and Imaginary (b) Parts of I_ρ^H for $\epsilon_1/\epsilon_o = 16$, $\sigma_1 = 0$.

These were determined by numerical tests to keep relative errors of interpolation generally in the range of 10^{-3} to 10^{-4}. A smaller ΔR_1 could be needed in grid 2 for large ϵ_1 and small σ_1 to handle the rapidly oscillating evanescent wave, but this is easily changed in the code.

The field evaluation in NEC uses variable-interval-width Romberg integration over the current distribution. At each integrand evaluation, the components I_ρ^V, I_z^V, I_ρ^H, and I_ϕ^H are obtained by interpolation, and the field components are combined according to the direction of the current. The numerical integral is then combined with the free-space field and with the image field multiplied by $(k_1^2 - k_2^2)/(k_1^2 + k_2^2)$ to obtain the total field over ground.

When R_1 from the observation point to the center of a wire segment is greater than one wavelength, the field is evaluated by Norton's asymptotic approximations (ref. 26) rather than the above method. Norton's formulas are given in Part II of this manual under subroutine GWAVE. Although they are less accurate than the Sommerfeld integral forms and require longer to evaluate than the interpolation, their use permits truncating the interpolation tables. Another approximation used for R_1 greater than a wavelength is to treat the current distribution on a segment as a lumped current element with the correct moment rather than integrating over the current distribution.

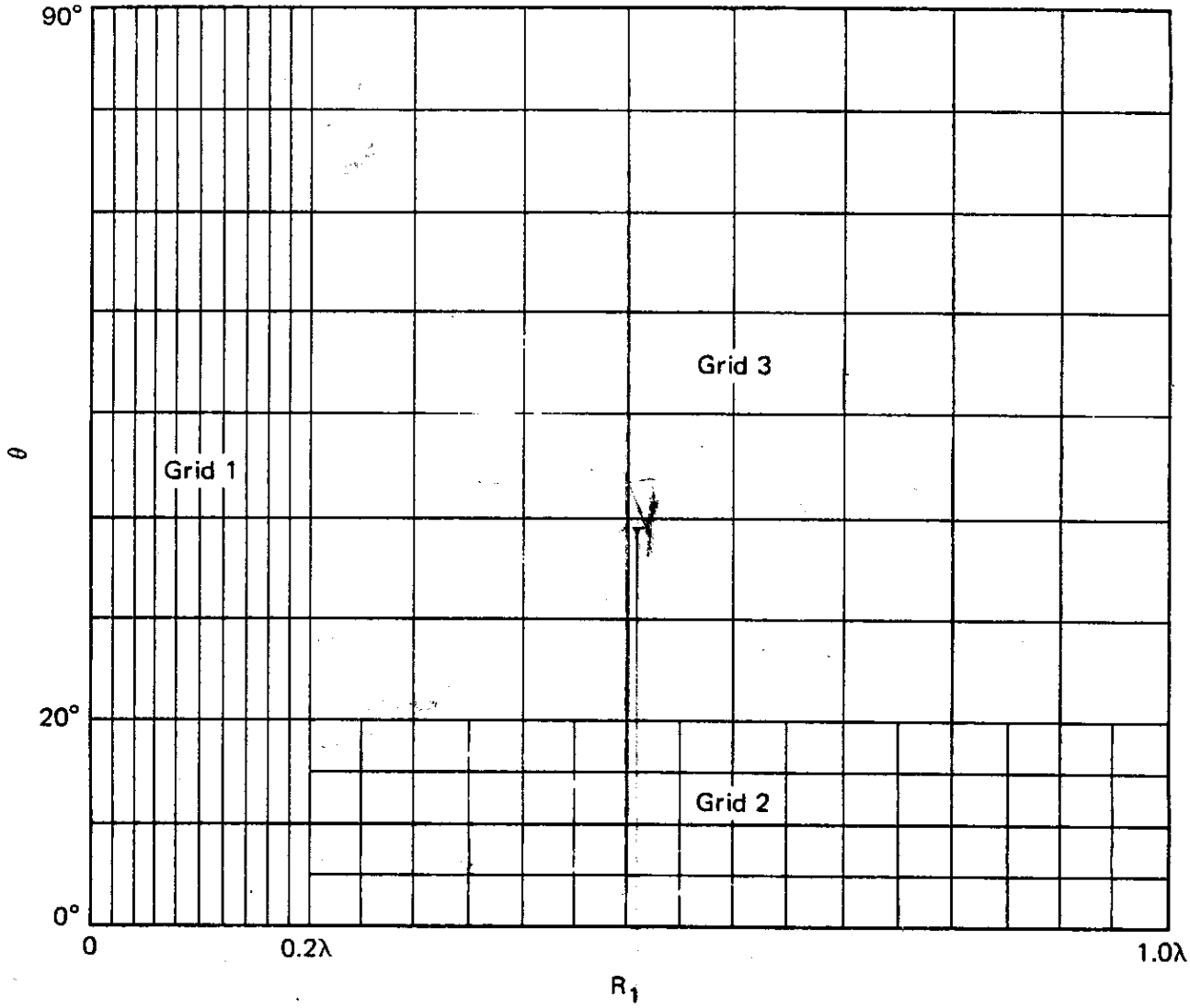

Fig. 12. Grid for Bivariate Interpolation of I's.

2. NUMERICAL EVALUATION OF THE SOMMERFELD INTEGRALS

The integrals in equations (148) through (153) are evaluated by numerical integration along contours in the complex λ plane. Although these integrals differ from the usual Sommerfeld integrals in the D_1 and D_2 terms, they are the same in the properties important to numerical integration — the locations of poles and branch cuts and the exponential behavior of the Bessel and exponential functions. The behavior of the integrands and numerical methods for evaluating the integrals are discussed in detail by Lytle and Lager

(ref. 27). This section describes the particular method used in NEC, which is basically the same as in the code WFLLL2A.

Since the integrands of the six integrals are similar, V'_{22} will be considered as typical. The integrands have branch cuts from $\pm k_1$ to infinity and $\pm k_2$ to infinity due to the square roots in γ_1 and γ_2 respectively. The branch cuts are chosen to be vertical, as shown in figure 13. The implications of this choice of branch cuts and the choice of Reimann sheets are discussed in ref. 27.

The key to rapid convergence in the numerical integration is to exploit the exponential behavior of the exponential and Bessel functions for large λ. The integration contour is deformed from the real axis into the complex plane, avoiding branch cuts and taking account of poles, to optimize convergence. With the vertical branch cuts chosen, there are no real poles on the primary Reimann sheet although virtual poles from D_1 or D_2 result in a near singularity in the region of $\pm k_2$ when k_1 approaches k_2 (free-space limit). Hence the integration contour should avoid the real axis in this region.

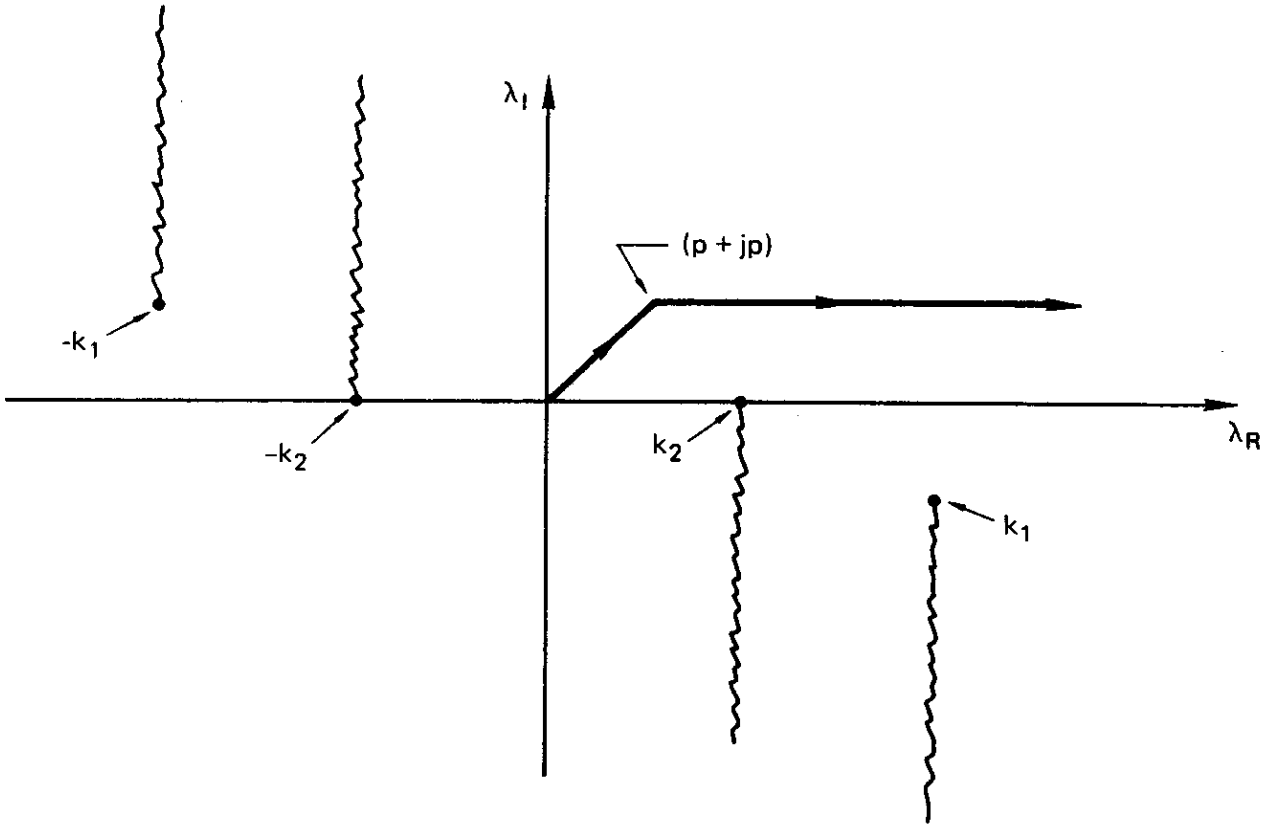

Figure 13. Contour for Evaluation of Bessel Function Form of Sommerfeld Integrals.

The contour used with the form of the integrals in equations (148) through (153) is shown in figure 13. The dominant factor for convergence in this case is the exponential function as λ_R increases. The Bessel function oscillates with slow convergence for increasing λ_R and grows exponentially as $|\lambda_I|$ increases. Hence it is of little help in convergence but restricts the contour to small $\rho|\lambda_I|$. The break in the contour is at $\lambda = p + jp$ where p is the minimum of $1/\rho$ and $1/(z + z')$.

Integration along this contour becomes difficult when $(z + z')/\rho$ is small since there may be many oscillations of the Bessel function before convergence. In this case an alternate form of the integrals is used which for V'_{22} is

$$V'_{22} = \frac{1}{2}\int_{-\infty}^{\infty} D_2 \exp\left[-\gamma_2(z + z')\right] H_o^{(2)}(\lambda\rho)\lambda d\lambda \ . \qquad (173)$$

Since the Hankel function of type 2 decays exponentially as λ_I becomes negative, it provides rapid convergence without the $\exp -\gamma_2(z + z')$ factor. The behavior of the integrand can be seen from the large argument approximation

$$\exp\left[-\gamma_2(z + z')\right] H_o^{(2)}(\lambda\rho) \approx \sqrt{\frac{2j}{\pi\lambda\rho}} \left\{\exp -\lambda[\pm (z + z') + j\rho]\right\} \ ,$$

where, for the vertical branch cuts, the ± sign is

$$+ \text{ for } \lambda_R > -k_2 \text{ and } \lambda_I > 0 \ ,$$
$$+ \text{ for } \lambda_R > k_2 \text{ and } \lambda_I < 0 \ ,$$
$$- \text{ otherwise.}$$

Thus, an integration path having

$$\lambda_I < 0$$

and

$$\lambda_I/\lambda_R = -\rho/(z + z') \text{ for } \lambda_R > k_2$$

or

$$\lambda_I/\lambda_R = \rho/(z + z') \text{ for } \lambda_R < k_2$$

results in exponential convergence with little oscillation. The basic contour used with the Hankel function form is shown in figure 14 where

$$a = -j\ 0.4\ k_2 \ ,$$
$$b = (0.6 + j\ 0.2)k_2 \ ,$$

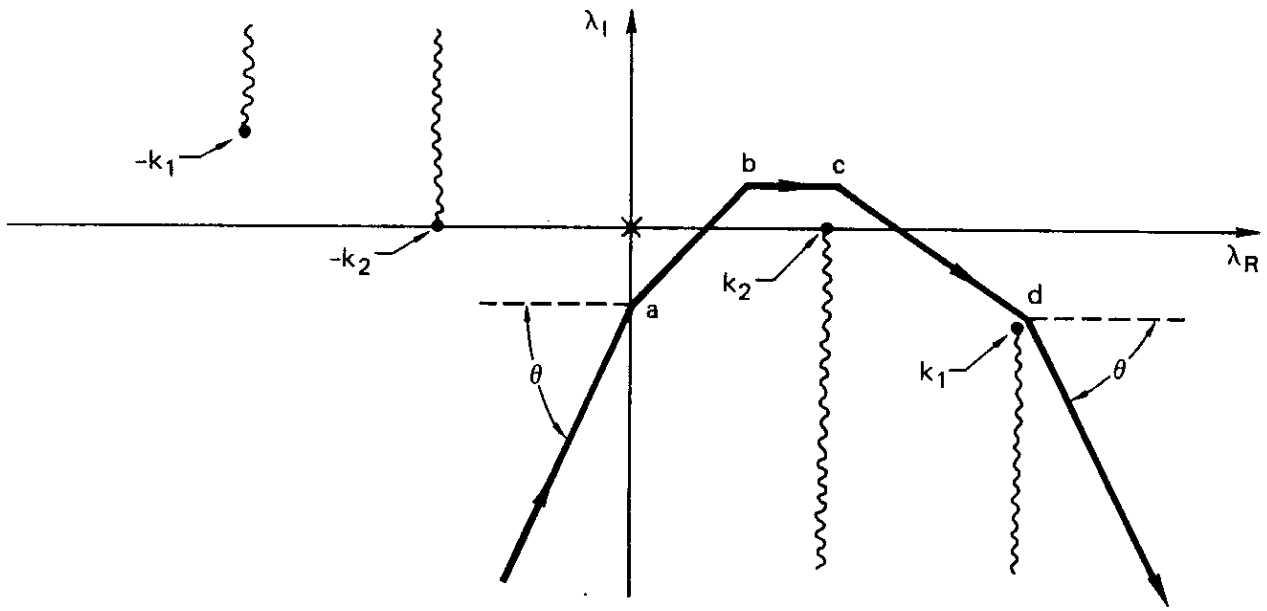

Figure 14. Contour for Evaluation of Hankel Function Form of Sommerfeld Integrals.

$$c = (1.02 + j\ 0.2)k_2 \ ,$$
$$d = 1.01\ k_{1_R} + j\ 0.99\ k_{1_I} \ ,$$
$$\theta = \tan^{-1}\left(\frac{\rho}{z + z'}\right) \ .$$

To avoid the near singularity as k_1 approaches k_2, the real part of d is not allowed to be less than 1.1 k_2. This contour provides rapid convergence except when $z + z'$ is small, $|k_1\rho|$ is large, and k_{1_I}/k_{1_R} is small. There may then be many oscillations between c and d with little convergence. In such a case the contour in figure 15 is used where

$$e = k_1 + (-0.1 + j\ 0.2) \ ,$$
$$f = k_1 + (0.1 + j\ 0.2) \ .$$

The Hankel function form of the integrals provides rapid convergence for small $z + z'$ including the case of $z = z' = 0$. For small ρ, however, the pole at $\lambda\rho = 0$ requires special treatment. In NEC the Hankel function form with the contour of figure 14 or 15 is used when ρ is greater than $(z + z')/2$ and the Bessel function form is used otherwise.

Integration along the contours is accomplished by adaptive interval-width Romberg integration. On the sections going to infinity, adaptive Romberg

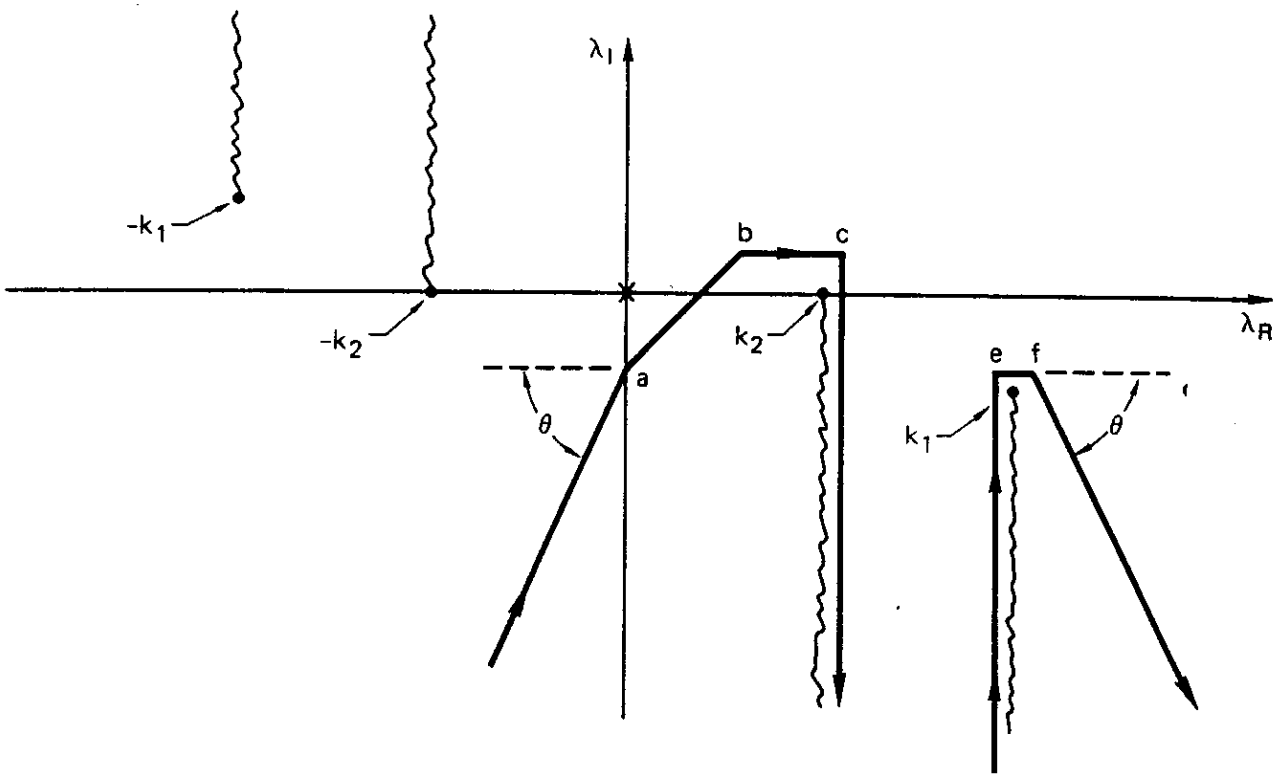

Figure 15. Contour for Hankel Function Form when Real Part k_1 is Large and Imaginary Part k_1 is Small.

integration is applied to successive subsections of length p, where p is the minimum of $0.2\pi/\rho$ or $0.2\pi/(z + z')$, and Shanks' nonlinear transformation (ref. 28) is applied to the sequence of partial sums to accelerate convergence. When ρ and $z + z'$ are both small, the integration interval, p, may be large since the exponential and Bessel functions change slowly and the remaining factors are easily integrated once λ becomes large. For the Bessel function form of the integrals the minimum for $R_1 = [\rho^2 + (z + z')^2]^{1/2}$ is limited only by the maximum number size for the computer. For the Hankel function form the minimum R_1 is about 10^{-5} wavelengths due to the pole at $\lambda\rho = 0$. Either ρ or $z + z'$ may be zero.

The numerical integration results for small R_1 were checked against results from a series approximation (ref. 25) and were in very close agreement. For larger values of R_1 the results from different integration contours were compared as a validation test. Results for the modified Sommerfeld integrals were also checked with normal integrals used in the code WFLLL2A. Earlier studies for the code WFLLL2A, which is capable of computing the field across

the interface, verified the continuity of the computed tangential E field across the interface (ref. 44).

The average time required to evaluate the integrals for a given ρ and $z + z'$ on a CDC 7600 computer is about 0.06 s. Thus about 15 s are required to fill the interpolation grid. Once the grid has been computed and stored, the time to fill an interaction matrix, using interpolation and the Norton formulas, is about four times that for free space.

3. THE IMAGE AND REFLECTION-COEFFICIENT METHODS

The use of a reflected image is a simple and fast way to model the effect of a ground plane. If the ground is perfectly conducting, the structure and its image are exactly equivalent to the structure over the ground. Since use of the image only doubles the time to compute the field, it is always used with a perfect ground. NEC also includes an image approximation for a finitely conducting ground in which the image fields are modified by the Fresnel plane-wave reflection coefficients. Although this is far from exact for a finite ground, it has been shown to provide useful results for structures that are not too near to the ground (refs. 21 and 22). When it can be used, the reflection coefficient method is about twice as fast as the Sommerfeld/Norton method and avoids the need of computing the interpolation grid.

Implementation of the image and reflection coefficient methods in the code is very simple. The Green's function for a perfectly conducting ground is the sum of the free-space Green's function of the source current element and the negative of the free-space Green's function of the image of the source reflected in the ground plane. For the electric field, with free-space Green's dyad $\overline{\overline{G}}\ (\vec{r},\vec{r}')$ defined in equation (1), the Green's dyad for a perfect ground is

$$\overline{\overline{G}}_{pg}(\vec{r},\vec{r}') = \overline{\overline{G}}\ (\vec{r},\vec{r}') + \overline{\overline{G}}_I\ (\vec{r},\vec{r}')\ , \tag{174}$$

where

$$\overline{\overline{G}}_I\ (\vec{r},\vec{r}') = -\overline{\overline{I}}_r \cdot \overline{\overline{G}}\ (\vec{r},\overline{\overline{I}}_r \cdot \vec{r}')\ , \tag{175}$$

$$\overline{\overline{I}}_r = \hat{x}\hat{x} + \hat{y}\hat{y} - \hat{z}\hat{z}\ .$$

$\overline{\overline{I}}_r$ is a dyad that produces a reflection in the $z = 0$ plane when used in a dot product. For the magnetic field with free-space Green's dyad

$$\overline{\overline{\Gamma}}\ (\vec{r},\vec{r}') = \overline{\overline{I}} \times \nabla'\ g\ (\vec{r},\vec{r}') \tag{176}$$

the Green's dyad over a perfect ground is

$$\overline{\overline{\Gamma}}_{pg} = \overline{\overline{\Gamma}}(\vec{r},\vec{r}') + \overline{\overline{\Gamma}}_I(\vec{r},\vec{r}') \tag{177}$$

$$\overline{\overline{\Gamma}}_I(\vec{r},\vec{r}') = -\overline{\overline{I}}_r \cdot \overline{\overline{\Gamma}}(\vec{r},\overline{\overline{I}}_r \cdot \vec{r}') \tag{178}$$

The reflection coefficient method for finitely conducting ground uses the image fields modified by the Fresnel reflection coefficients. The Fresnel reflection coefficients, which are strictly correct only for an infinite plane-wave field, depend on the polarization of the incident field with respect to the plane of incidence (i.e., the plane containing the normal to the ground and the vector in the direction of propagation of the wave). The two cases are illustrated in figure 16 where the wave with E in the plane of incidence is termed vertically polarized and E normal to the plane of incidence as horizontally polarized. The Fresnel reflection coefficient for vertically polarized waves is

$$R_V = \frac{\cos\Theta - Z_R\sqrt{1 - Z_R^2 \sin^2\Theta}}{\cos\Theta + Z_R\sqrt{1 - Z_R^2 \sin^2\Theta}}, \tag{179}$$

where

$$\cos\Theta = -\hat{\kappa} \cdot \hat{z},$$

$$Z_R = \left(\frac{\varepsilon_1}{\varepsilon_o} - j\frac{\sigma_1}{\omega\varepsilon_o}\right)^{-1/2}.$$

The reflected fields are then

$$\vec{E}_R^V = -R_V\left(\overline{\overline{I}}_R \cdot \vec{E}^V\right),$$

$$\vec{H}_R^V = R_V \vec{H}^V.$$

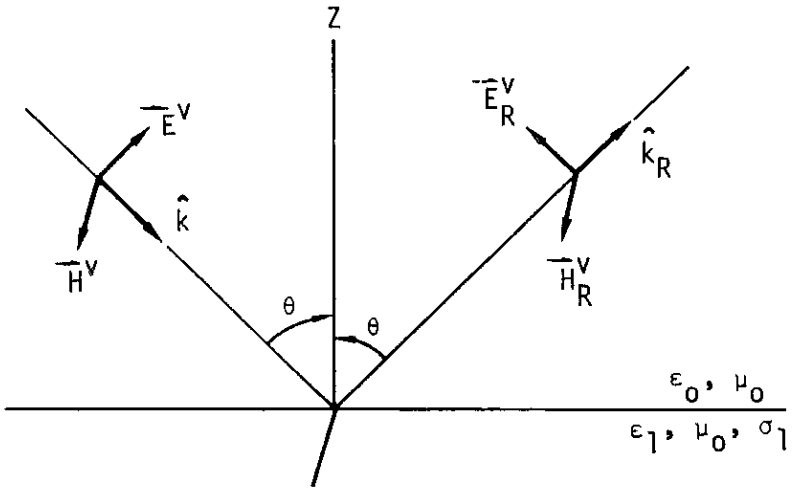

Reflection of Vertically Polarized Wave

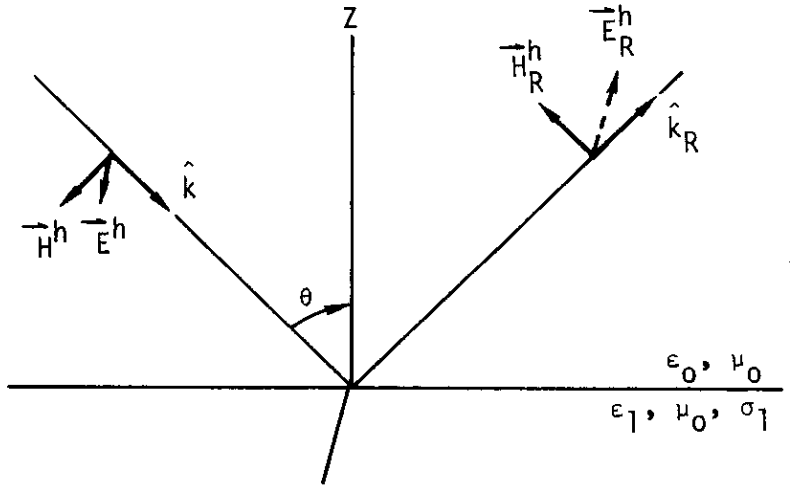

Reflection of Horizontally Polarized Wave

Figure 16. Plane-Wave Reflection at an Interface.

For horizontally polarized waves, the reflection coefficient is

$$R_H = \frac{-\left(Z_R \cos\Theta - \sqrt{1 - Z_R^2 \sin^2\Theta}\right)}{Z_R \cos\Theta + \sqrt{1 - Z_R^2 \sin^2\Theta}} , \tag{180}$$

and

$$\vec{E}_R^h = - R_H \vec{E}^h ,$$

$$\vec{H}_R^h = R_H \left(\bar{\bar{I}}_R \cdot \vec{H}^h\right) .$$

An arbitrarily polarized incident plane wave must be resolved into horizontal and vertical components to determine the reflected field. Thus, if $\hat{p}$ is the unit vector normal to the plane of incidence, the reflected field due to an incident field $\vec{E}$ is

$$\begin{aligned} \vec{E}_R &= R_H(\vec{E}_I \cdot \hat{p})\hat{p} + R_V \left[\vec{E}_I - (\vec{E}_I \cdot \hat{p})\hat{p}\right] \\ &= R_V \vec{E}_I + (R_H - R_V)(\vec{E}_I \cdot \hat{p})\hat{p} , \end{aligned} \tag{181}$$

where $\vec{E}_I$ is the incident field reflected in a perfectly conducting ground, or the field due to the image of the source. Use of the image field in equation (181) accounts for the changes in sign and vector direction of the incident field that were shown explicitly for the vertically and horizontally polarized cases. For the magnetic field,

$$\vec{H}_R = R_H \vec{H}_I + (R_V - R_H)(\vec{H}_I \cdot \hat{p})\hat{p} , \tag{182}$$

with $\vec{H}_I$ the field of the image of the source.

Applying the Fresnel reflection coefficients to the near fields, the electric field at $\vec{r}$ due to the image of a current element at $\vec{r}'$ can be written

$$\begin{aligned} \bar{\bar{G}}_R(\vec{r},\vec{r}') &= R_V \bar{\bar{G}}_I(\vec{r},\vec{r}') \\ &\quad + (R_H - R_V)\left[\bar{\bar{G}}_I(\vec{r},\vec{r}') \cdot \hat{p}\right]\hat{p} , \end{aligned} \tag{183}$$

where

$$\hat{p} = \vec{p}/|\vec{p}| \ ,$$

$$\vec{p} = (\vec{r} - \vec{r}') \times \hat{z} \ ,$$

and $\overline{\overline{G}}_I$ is the Green's function for the image of the source in a perfect ground as defined in equation (175). For magnetic field, the Green's dyad for the modified image is

$$\overline{\overline{\Gamma}}_R(\vec{r},\vec{r}') = R_H \overline{\overline{\Gamma}}_I(\vec{r},\vec{r}') + (R_V - R_H)\left[\overline{\overline{\Gamma}}_I(\vec{r},\vec{r}') \cdot \hat{p}\right]\hat{p} \ . \tag{184}$$

The Green's functions for electric and magnetic fields over an imperfectly conducting ground, resulting from the reflection coefficient approximation are then

$$\overline{\overline{G}}_g(\vec{r},\vec{r}') = \overline{\overline{G}}(\vec{r},\vec{r}') + \overline{\overline{G}}_R(\vec{r},\vec{r}') \ , \tag{185}$$

$$\vec{\Gamma}_g(\vec{r},\vec{r}') = \overline{\overline{\Gamma}}(\vec{r},\vec{r}') + \overline{\overline{\Gamma}}_R(\vec{r},\vec{r}') \ . \tag{186}$$

Use of the Green's function's $\overline{\overline{G}}_g$ and $\overline{\overline{\Gamma}}_g$ results in a straightforward extension of the EFIE and MFIE for structures over an imperfect ground.

NEC also includes a reflection coefficient approximation for a radial wire ground screen, as used by Miller and Deadrick (ref. 29). This is based on an approximation developed by Wait (ref. 30) for the surface impedance of the radial-wire ground screen on an imperfectly conducting ground, as the parallel combination of the surface impedance, ζ_1, of the ground plane

$$\zeta_1 = \left(\frac{j\mu_o\omega}{\sigma_1 + j\varepsilon_1\omega}\right)^{1/2} \ ,$$

and an approximate surface impedance Z_g of the ground screen

$$Z_g(\rho) = \frac{j\mu_o\omega\rho}{N} \ln\left(\frac{\rho}{NC_o}\right) \ .$$

The ground screen impedance assumes a parallel wire grid having the wire spacing that the radial wires have at a distance ρ from the center. N is the number of radial wires in the screen, and C_o is the radius of the wires. The surface impedance of the ground screen on an imperfect ground is then

$$\zeta_e = \frac{\zeta_1 Z_g}{\zeta_1 + Z_g} .$$

From the definition of surface impedance,

$$E_{tangential} = \zeta_e H_{tangential}$$

at the surface. Using the fact that E and H in the incident wave are related by η the free-space impedance, reflection coefficients are derived as

$$R_H = \frac{\eta - \zeta_e \cos \Theta}{\eta + \zeta_e \cos \Theta} ,$$

and

$$R_V = \frac{\eta \cos \Theta - \zeta_e}{\eta \cos \Theta + \zeta_e} .$$

This is the form the Fresnel reflection coefficients take when the index of refraction is large compared to unity ($|Z_R|^2 << 1$). This condition is satisfied in most realistic problems; furthermore, the surface-impedance boundary condition is a valid approximation only when the refractive index of the ground is large compared to unity. The surface impedance is used in conjunction with the reflection coefficient method previously discussed to provide an approximate model of a radial-wire ground screen.

Due to the assumption of specular reflection, only the properties of the ground directly under a vertical antenna will affect its current distribution. At the origin of the radial-wire ground screen, the impedance is zero (Z_g is not allowed to be negative) so the impedance and current distribution of a vertical antenna at the origin will be the same as over a perfect conductor. The far fields, however, will demonstrate the effect of the screen as the specular point moves away from the origin. For antennas other than the vertical

antenna, it should be pointed out that the inherent polarization sensitivity of the screen (i.e., E parallel or perpendicular to the ground wires) has not been considered in this approximation. When limited accuracy can be accepted this ground screen approximation provides a large time saving over explicit modeling with the Sommerfeld/Norton method since the ground screen does not increase the number of unknowns in the matrix equation.

Section V
Modeling of Antennas

Previous sections have dealt with the problem of determining the current induced on a structure by an arbitrary excitation. We now consider some specific problems in modeling antennas and scatterers, including models for a voltage source on a wire, lumped and distributed loads, nonradiating networks, and transmission lines. Calculations of some observable quantities are also covered including input impedance, radiated field, and antenna gain.

1. SOURCE MODELING

The approach used in NEC is applicable to a number of electromagnetic analysis problems. For receiving antennas and EMP studies, the excitation is the field of an incident plane wave and the desired response is the induced current at one or more points on the structure. In scattering analysis the excitation is still an incident plane wave, but the desired response is the field radiated by the induced currents. In the case of a wire transmitting antenna, however, the excitation is generally a voltage source on the wire. The antenna source problem has received a considerable amount of attention in the literature. A rather thorough exposition on the appropriate source configuration for the linear dipole antenna has been given by King (ref. 31). The delta-function source, which may be visualized as an infinitesimally thin, circumferential belt of axially directed electric field [or, alternatively, as a frill of magnetic current at the antenna feed point (ref. 32)], is convenient mathematically, but of somewhat questionable physical realizability. Since the excitation can be specified only at discrete points in NEC, a delta-function source is not feasible.

A useful source model, however, is an electric field specified at a single match point. For a voltage source of strength V on segment i, the element in the excitation vector corresponding to the applied electric field at the center of segment i is set to

$$E_i = \frac{V}{\Delta_i} \quad , \tag{187}$$

where Δ_i is the length of segment i. The direction of E_i is toward the positive end of the voltage source so that it pushes charge in the same direction as the source. The field at other match points is set to zero.

The actual effective voltage is the line integral of the applied field along the wire. This cannot be determined beforehand since the field is known only at segment centers, but can be determined after the solution for current by integrating the scattered field produced by the current. For equal length segments in the vicinity of the source this field, which must be the negative of the applied field at every point on the wire, is nearly constant over segment i and drops sharply at the segment ends. This results in an actual voltage of approximately $\Delta_i E_i$ as assumed in equation (187). When the source segment and adjacent segments are not of equal length, however, the actual voltage, obtained by integrating the scattered field, may differ from the intended value.

Ideally, this source model applies a voltage V between the ends of the source segment. Hence, the antenna input admittance could be computed as the current at the segment ends or, in an unsymmetric case, the average of the current at the two ends, divided by the applied voltage. In practice the segment is sufficiently short so that the current variation over its length is small and the current at the center can be used rather than the ends. When segment lengths in the source region are unequal, the computed input admittance may be inaccurate due to the discrepancy between the actual and assumed voltages. Use of the actual voltage, obtained by integrating the near field, will generally give an accurate admittance although it will require additional effort for computation.

An alternate source model that is less sensitive to the equality of segment lengths in the source region is based on a discontinuity in the derivative of current. This source model is similar to one used by Andreasen and Harris (ref. 33), and its use in a program similar to NEC was reported by Adams, Poggio, and Miller (ref. 24). For this model, the source region is viewed as a biconical transmission line with feed point at the source location, as illustrated in figure 17. The voltage between a point at s and the symmetric point on the other side of the line is then related to the derivative of the current by the transmission line equation,

$$V(s) = - jZ_o \frac{\partial I(ks)}{\partial (ks)} \quad , \tag{188}$$

where Z_o is the characteristic impedance of the transmission line. The characteristic impedance of a biconical transmission line of half-angle Θ is

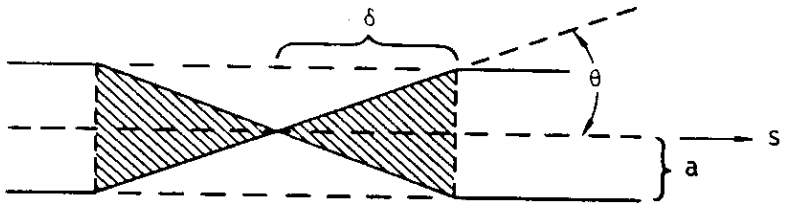

Figure 17. Biconical Transmission Line Model of Source Region.

$$Z_o = 120\ \ell n\left(\cot\frac{\Theta}{2}\right) ,$$

or for small angles,

$$Z_o \approx 120\ \ell n\left(\frac{2}{\Theta}\right) . \tag{189}$$

For a source on a wire, however, the proper choice for δ in figure 17, defining the angle Θ, is unclear. Adams at al. (ref. 24) used an average value of Z_o obtained by averaging equation (189) for δ ranging from zero to d as

$$Z_{avg} = \frac{1}{d}\int_o^d 120\ \ell n\left(\frac{2\delta}{a}\right) d\delta$$

$$= 120\left[\ell n\left(\frac{2d}{a}\right) - 1\right] ,$$

where d is set equal to the distance from the source location at the segment end to the match point at the segment center. The voltage across the line is then

$$V(s) = -\,j\ 120\left[\ell n\left(\frac{2d}{a}\right) - 1\right]\frac{\partial I(ks)}{\partial(ks)} .$$

Allowing for a current unsymmetric about the source, the voltage V_o of a source at s_o is related to a discontinuity in current derivative as

$$\lim_{\varepsilon\to o}\left[\left.\frac{\partial I(ks)}{\partial(ks)}\right|_{s = s_o + \varepsilon} - \left.\frac{\partial I(ks)}{\partial(ks)}\right|_{s = s_o - \varepsilon}\right] =$$

$$\frac{-jV_o}{60\left[\ell n\left(\frac{2d}{a}\right) - 1\right]} . \tag{190}$$

This discontinuity in current derivative is introduced into NEC by modifying the current expansion on the wire. The normal expansion for N_s wire segments is

$$I(s) = \sum_{j=1}^{N_s} \alpha_j \, f_j(s) \ ,$$

where the basis functions, f_j, are defined in section III-1 such that I(s) has continuous value and derivative along wires, and satisfies Kirchoff's law and a condition on charge density at junctions.

For a current-slope-discontinuity source at the first end of segment ℓ, the current expansion is modified to

$$I(s) = \sum_{j=1}^{N_s} \alpha_j \, f_j(s) + \beta_\ell \, f_\ell^*(s) \ , \qquad (191)$$

where f_ℓ^* is a basis function for segment ℓ, as defined in section III-1, but computed as if the first end of segment ℓ were a free end and the segment radius were zero. Hence, f_ℓ^* goes to zero with nonzero derivative at the source location.

If f_ℓ^* on segment ℓ is

$$f_\ell^*(s) = A_\ell^* + B_\ell^* \sin k(s - s_\ell) + C_\ell^* \cos k(s - s_\ell)$$

$$\times \, |s - s_\ell| < \Delta_\ell/2 \ ,$$

then

$$\frac{\partial}{\partial(ks)} \, f_\ell^*(s) \Big|_{\, s \, = \, s_\ell \, - \, \Delta_\ell/2} = B_\ell^* \cos(k\Delta_\ell/2) + C_\ell^* \sin(k\Delta_\ell/2) \ .$$

Since the sum of the normal basis functions has continuous value and derivative at $s = s_\ell - \Delta_\ell/2$, the current in equation (191) has a discontinuity in derivative of

$$\lim_{\varepsilon \to o} \left\{ \frac{\partial}{\partial(ks)} \, I(s) \Big|_{s = s_\ell \, - \, \Delta_\ell/2 \, + \, \varepsilon} - \frac{\partial}{\partial(ks)} \, I(s) \Big|_{s = s_\ell \, - \, \Delta_\ell/2 \, - \, \varepsilon} \right\} =$$

$$\beta_\ell \left\{ B_\ell^* \cos(k\Delta_\ell/2) + C_\ell^* \sin(k\Delta_\ell/2) \right\} .$$

Hence, from equation (190), a source voltage of V_o requires a value of β_ℓ in the current expansion of

$$\beta_\ell = \frac{-jV_o}{60} \left\{ \left[\ell n\left(\frac{\Delta_\ell}{a_\ell}\right) - 1 \right] \left[B_\ell^* \cos(k\Delta_\ell/2) + C_\ell^* \sin(k\Delta_\ell/2) \right] \right\}^{-1} . \tag{192}$$

The linear system for the current expansion constants, obtained by substituting equation (191) for f in equation (18), is

$$\sum_{j=1}^{N_s} \alpha_j \langle w_i, Lf_j \rangle = \langle w_i, e \rangle - \beta_\ell \langle w_i, f_\ell^* \rangle . \tag{193}$$

$$i = 1, \ldots N_s$$

In matrix notation, corresponding to equation (19),

$$[G]\ [A] = [E] + \beta_\ell\ [F] , \tag{194}$$

where F_i is the excitation for segment or patch equation number i due to the field of f_ℓ^*, and E_i is the excitation for segment or patch equation number i from other sources (if there are any). The interaction matrix G is independent of this source as it is of other sources. The solution for the expansion coefficients is then

$$[A] = [G^{-1}] \left\{ [E] + \beta_\ell\ [F] \right\} ,$$

where A supplies the coefficients α_j in equation (191) to determine the current. This method is easily extended to several sources. The modified basis function f_ℓ^* appears to introduce an asymmetry into the current, but this is not the case since the other basis function amplitudes are free to adjust accordingly.

The current-slope-discontinuity source results in an effective applied field that is much more localized in the source region than that of the constant-field source defined by equation (187). The difference is shown in near-field plots for the two source models in figure 18, taken from Adams

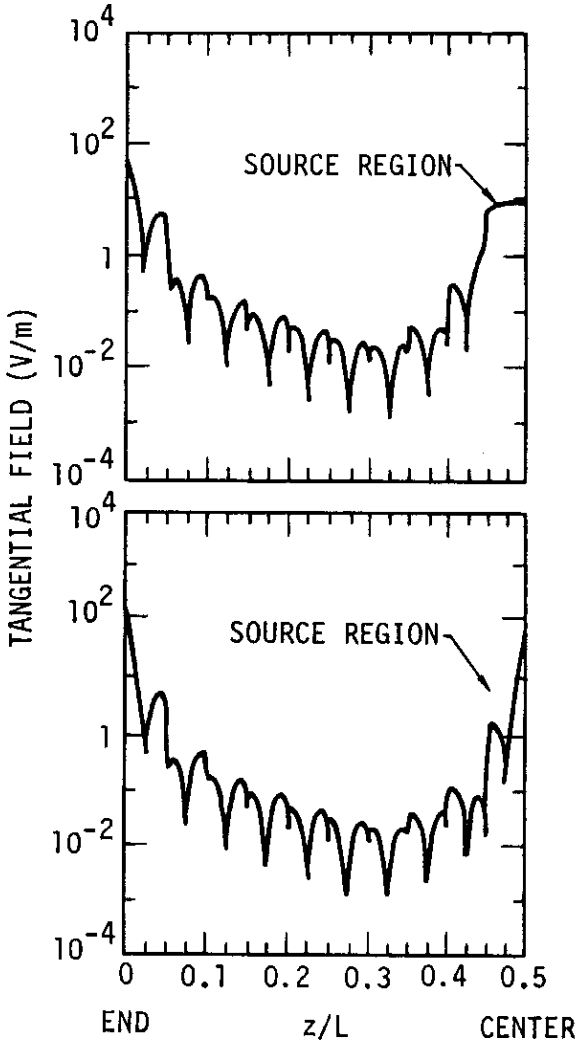

Figure 18. Field Plots for a Linear Dipole, Ω=15.

et al. (ref. 24). The near fields are for a half wavelength dipole antenna with $\Omega = 15$ [$\Omega = 2\ell n(L/a)$, L = length, a = radius] and with 10 segments on half of the antenna covered by the plots. The constant-field source is seen to result in a nearly rectangular field distribution in the source region while the field of the slope-discontinuity source approaches a delta function. The integrals of these two source-field distributions yield approximately the same voltages, however.

With the slope-discontinuity-source model, the input admittance is the ratio of the current at the segment end, where the source is located, to the source voltage. Adams et al. also present results showing the effect on admittance of varying the source-segment length relative to the lengths of adjacent segments, showing that the slope-discontinuity source is much less sensitive to segment length than is the constant-field source. The two segments on opposite sides of the source must have equal lengths and radii, however. For very short segment lengths, the slope-discontinuity model may break down although, as with the constant-field source, the correct admittance can be obtained by integrating the near field to obtain the source voltage.

2. NONRADIATING NETWORKS

Antennas often include transmission lines, lumped circuit networks, or a combination of both connecting between different parts or elements. When the currents on transmission lines or at network ports are balanced, the resulting fields cancel and can often be neglected, greatly simplifying the

modeling problem. The solution procedure used in NEC is to compute a driving-point-interaction matrix from the complete segment-interaction matrix. The driving-point matrix relates the voltages and currents at network connection points as required by the electromagnetic interactions. The driving-point-interaction equations are then solved together with the network or transmission line equations to obtain the induced currents and voltages. In this way the larger segment-interaction matrix is not changed by addition or modification of networks or transmission lines.

The solution described below assumes an electromagnetic interaction matrix equation of the form,

$$[G]\ [I] = -\ [E]\ , \tag{195}$$

where E_i is the exciting electric field on wire segment i and I_i is the current at the center of segment i. In NEC the interaction equation has the form,

$$[G]\ [A] = -\ [E]\ ,$$

where A_i is the amplitude of the i^{th} basis function f_i in the current expansion,

$$I(s) = \sum_{i=1}^{N_s} A_i\ f_i(s)\ .$$

The same solution technique can be used, however, by computing I from A whenever I is needed. This must be done in computing the elements of the inverse of G, G^{-1}_{ij}, which below represent the current on segment i due to a unit field on segment j.

A model consisting of N_s segments will be assumed with a general M-port network connected to segments 1 through M. The network is described by the admittance equations,

$$\sum_{j=1}^{M} Y_{ij}\ V_j = I_i^t \qquad i=1,\ \ldots,\ M\ , \tag{196}$$

where V_i and I_i^t are the voltage and current at port i, with reference directions as shown in figure 19.

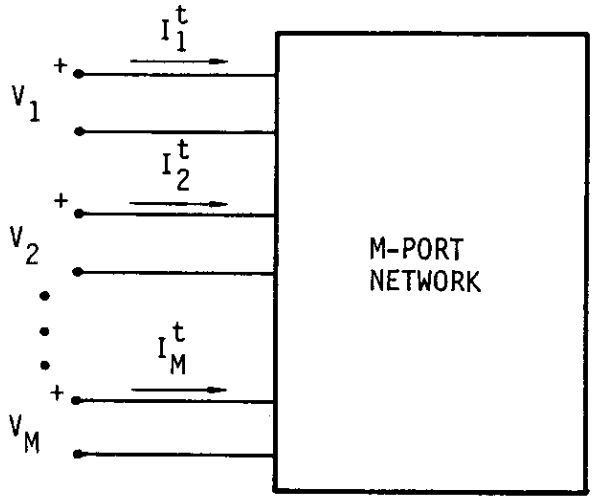

Figure 19. Voltage and current Reference Directions at Network Ports.

The connection of a network port to a segment is illustrated in figure 20. The segment is broken, and the port is connected so that

$$I_i^t = - I_i \ , \tag{197}$$

where I_i is the segment current. Figure 21 shows a voltage source of strength V_i connected across the network port at segment i. In this case,

$$I_i^t = I_i^g - I_i \ . \tag{198}$$

In either case, the port voltage may be related to the applied field on the segment by the constant-field voltage source model of equation (187).

We will assume that segments 1 through M_1 are connected to network ports without voltage sources, and segments $M_1 + 1$ through M are connected to network ports with voltage sources. The remaining segments have no network

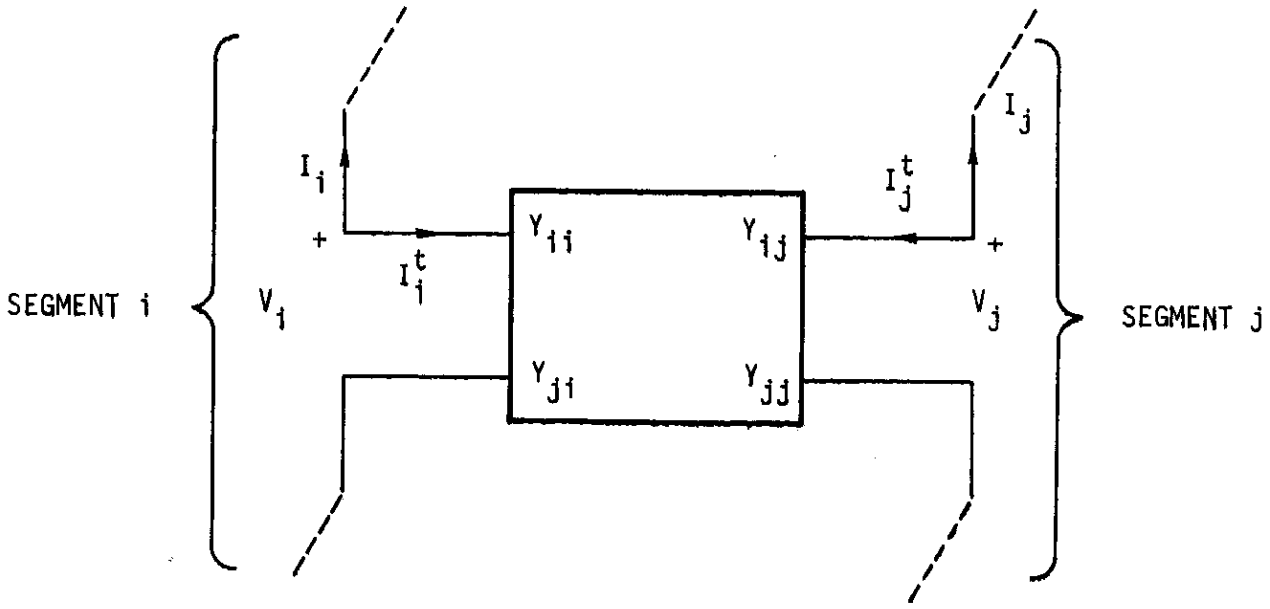

Figure 20. Network Connection to Segments.

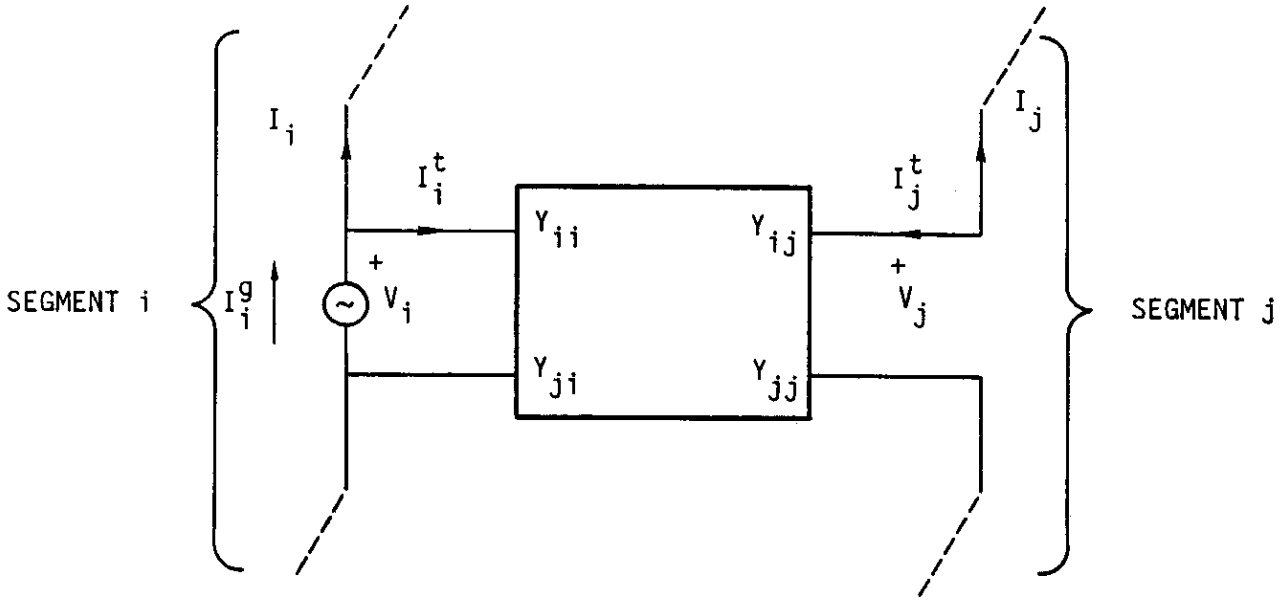

Figure 21. Network Port and Voltage Source Connected to a Segment.

connections but may have voltage sources. In addition all of the segments may be excited by an incident field represented by E_i^I on segment i. The total field on segment i is then

$$E_i = \frac{V_i}{\Delta_i} + E_i^I \ ,$$

where V_i is a gap voltage, due either to a network port or voltage source, and Δ_i is the segment length.

Equation (195) may be solved for current as

$$I_i = - \sum_{j=1}^{N_s} G_{ij}^{-1} E_j \qquad i=1, \ \ldots, \ N_s \ , \tag{199}$$

where G_{ij}^{-1} is the $(i,j)^{th}$ element of the inverse of matrix G. Before evaluating equation (199), however, the unknown port voltages, V_i, for $i = 1,\ldots,M_1$ must be determined. Hence, equation (199) is written with all known quantities on the right-hand side as

$$\sum_{j=1}^{M_1} G_{ij}^{-1} E_j^P + I_i = B_i \qquad i=1, \ \ldots, \ M_1 \ , \tag{200}$$

where

$$E_j^P = \frac{V_j}{\Delta_j} ,$$

and

$$B_i = - \sum_{j=1}^{M_1} G_{ij}^{-1} E_j^I - \sum_{j=M_1+1}^{N_s} G_{ij}^{-1} E_j .$$

Similarly, the network equations (196) are written using equation (197) as

$$\sum_{j=1}^{M_1} Y'_{ij} E_j^P + I_i = C_i \qquad i=1, \ldots, M_1 , \tag{201}$$

where

$$Y'_{ij} = \Delta_j Y_{ij} ,$$

$$C_i = - \sum_{j=M_1+1}^{M} Y_{ij} V_j .$$

The current is then eliminated between equations (200) and (201) to yield

$$\sum_{j=1}^{M_1} \left(G_{ij}^{-1} - Y'_{ij} \right) E_j^P = B_i - C_i \qquad i=1, \ldots, M_1 . \tag{202}$$

The solution procedure is then to solve equation (202) for E_j^P for $j = 1,\ldots,M_1$. Then, with the complete excitation vector determined, use equation (199) to determine I_i for $i = 1,\ldots,N_s$. Finally, the remaining network equations with equation (198) are used to compute the generator currents as

$$I_i^g = \sum_{j=1}^{M} Y_{ij} V_j + I_i \qquad i=M_1+1, \ldots M . \tag{203}$$

The currents I_i^g determine the input admittances seen by the sources.

In NEC the general M-port network used here is restricted to multiple two-port networks, each connecting a pair of segments.

3. TRANSMISSION LINE MODELING

Transmission lines interconnecting parts of an antenna may be modeled either explicitly by including the transmission line wires in the thin-wire model, or implicitly by the method described in the preceding section for nonradiating networks. For an implicit model, the short-circuit-admittance parameters of the transmission line viewed as a two-port network are

$$Y_{11} = Y_{22} = - j\, Y_o \cot(k\ell) ,$$

$$Y_{12} = Y_{21} = j\, Y_o \csc(k\ell) ,$$

where Y_o is the characteristic admittance of the line, k is the wave number $(2\pi/\lambda)$, and ℓ is the length of the line. If a separate admittance element is connected across the end of a transmission line, its admittance is added to the self-admittance of that network port.

The implicit model is limited, however, in that it neglects interaction between the transmission line and the antenna and its environment. This approximation is justified if the currents in the line are balanced, i.e., in a log periodic dipole antenna, and in general if the transmission line lies in an electric symmetry plane. The balance can be upset, however, if the transmission line is connected to an unbalanced load or by unsymmetric interactions. If the unbalance is significant, the transmission line can be modeled explicitly by including the wires in the thin-wire model. The explicit model is completely general, and yields accurate results since the sine, cosine, and constant current expansion in NEC is a good representation of the sinusoidal transmission line currents. The accuracy is demonstrated in figure 22 for transmission lines terminated in short circuit, open circuit, and matched loads.

The explicit transmission line model is, of course, less efficient in computer time and storage because of the additional segments required. In cases where the physical line presence does have a significant effect on the results, the effect may be modeled by explicitly modeling a single conductor of the line while using the implicit model to represent the balanced current component.

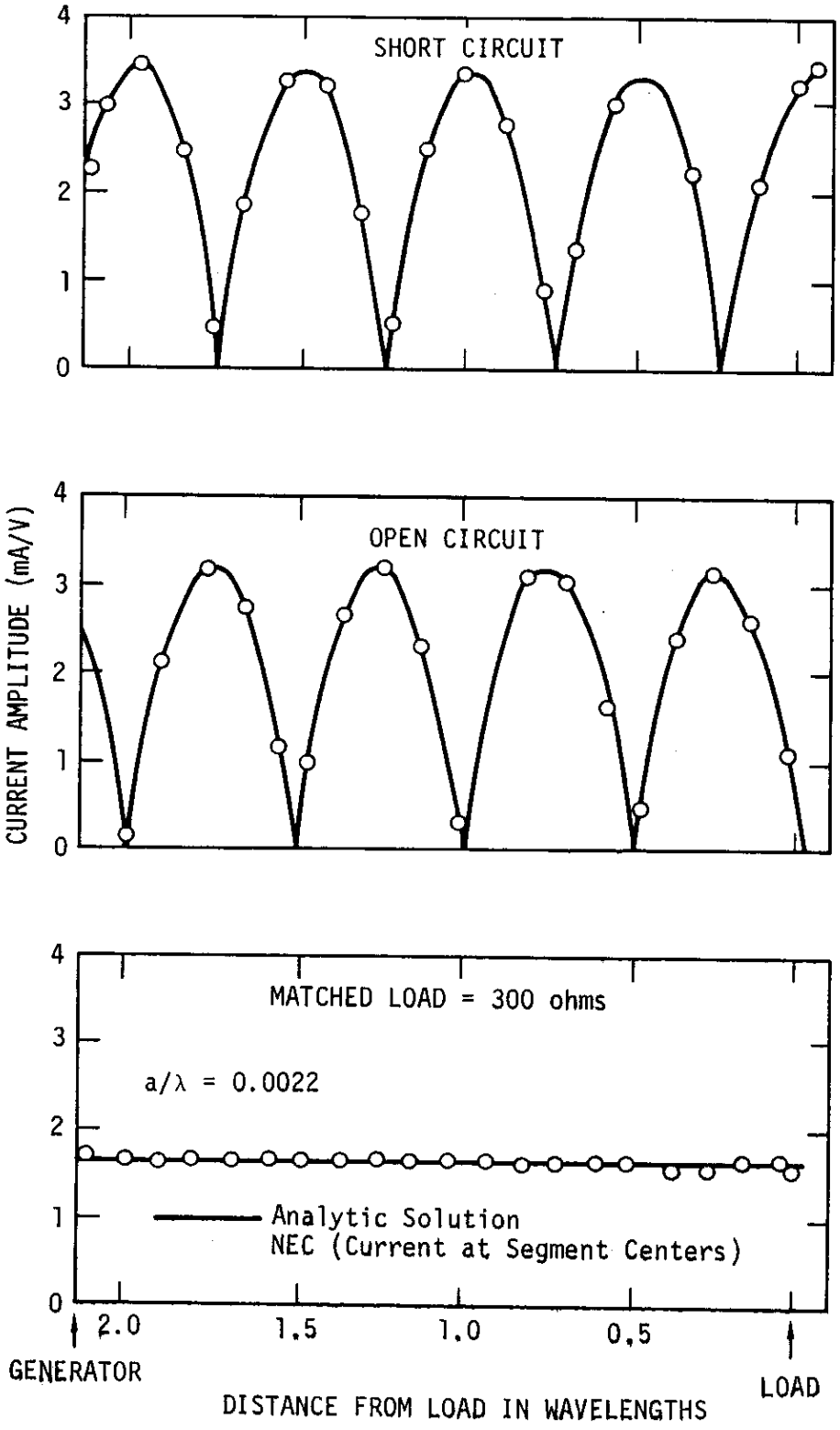

Figure 22. Current Distribution on a Two-Wire Transmission Line from NEC Compared with the Ideal Transmission Line Solution.

4. LUMPED OR DISTRIBUTED LOADING

Thus far, we have assumed that all structures to be modeled are perfect electric conductors. The EFIE is easily extended to imperfect conductors by modifying the boundary condition from equation (4) to

$$\hat{n}(\vec{r}) \times \left[\vec{E}^s(\vec{r}) + \vec{E}^I(\vec{r})\right] = Z_s(\vec{r})\left[\hat{n}(\vec{r}) \times \vec{J}_s(\vec{r})\right] ,$$

where $Z_s(\vec{r})$ is the surface impedance at $\vec{r}$ on the conducting surface. For a wire, the boundary condition is

$$\hat{s} \cdot \left[\vec{E}^s(\vec{r}) + \vec{E}^I(\vec{r})\right] = Z_w(s)\ I(s) ,$$

with $\vec{r}$ and $\hat{s}$ the position vector and tangent vector at s on the wire and $Z_w(s)$ the impedance per-unit-length at s. The matrix equation can then be written,

$$\sum_{j=1}^{N_s} G_{ij}\ \alpha_j = -E_i + \frac{Z_i}{\Delta_i} I_i \qquad i=1, \ldots, N_s , \tag{204}$$

where

α_j = amplitude of basis function j,

E_i = the incident field on segment i,

I_i = current at the center of segment i,

Z_i = total impedance of segment i,

Δ_i = length of segment i.

The impedance term can be viewed as a constant field model of a voltage source, as described in section V-1, where the voltage is proportional to current. It is assumed that the current is essentially constant, with value I_i, over the length of the segment, which is a reasonable assumption for the electrically short segments used in the integral equation solution.

The impedance term can be combined with the matrix by expressing I_i in terms of the α_j as

$$I_i = \sum_{j=1}^{N_s} \alpha_j \left(A_j^i + C_j^i \right) ,$$

where A_j^i and C_j^i are the coefficients of the constant and cosine terms, respectively, in the section of basis function j extending onto segment i. If basis function j does not extend onto segment i, then A_j^i and C_j^i are zero. The matrix equation modified by loading is then

$$\sum_{j=1}^{N_s} G'_{ij} \alpha_j = - E_i \qquad i=1, \ldots, N_s , \tag{205}$$

where

$$G'_{ij} = G_{ij} - \frac{Z_i}{\Delta_i} \left(A_j^i + C_j^i \right) . \tag{206}$$

For a lumped circuit element, Z_i is computed from the circuit equations. For a distributed impedance, Z_i represents the impedance of a length Δ_i of wire, which in the case of a round wire of finite conductivity is given by

$$Z_i = \frac{j\Delta_i}{a_i} \sqrt{\frac{\omega\mu}{2\pi\sigma}} \left[\frac{\mathrm{Ber}(q) + j\ \mathrm{Bei}(q)}{\mathrm{Ber}'(q) + j\ \mathrm{Bei}'(q)} \right] ,$$

where

$q = (\omega\mu\sigma)^{1/2}\ a_i$,

a_i = wire radius,

σ = wire conductivity,

Ber, Bei = Kelvin functions.

This expression takes account of the limited penetration of the field into an imperfect conductor.

5. RADIATED FIELD CALCULATION

The radiated field of an antenna or reradiated field of a scatterer can be computed from the induced current by using a simplified form of equation (1) valid far from the current distribution. The far-field approximation, valid when the distance from the current distribution to the observation

point is large compared to both the wavelength and the dimensions of the current distribution, treats the distance $|\vec{r} - \vec{r}'|$ as constant within the integral except in the phase term, $\exp(-jk|\vec{r} - \vec{r}'|)$. For a structure consisting of a wire portion with contour L and current distribution $\vec{I}(s)$, and a surface portion S with current $\vec{J}_s(\vec{r})$, the far-zone field is

$$\vec{E}(\vec{r}_o) = \frac{jk\eta}{4\pi} \frac{\exp(-jkr_o)}{r_o} \times \left\{ \int_L \left[\left(\hat{k} \cdot \vec{I}(s) \right) \hat{k} - \vec{I}(s) \right] \exp(j\vec{k}\cdot\vec{r}) ds + \int_S \left[\left(\hat{k}\cdot\vec{J}_s(\vec{r}) \right) \hat{k} - \vec{J}_s(\vec{r}) \right] \exp(j\vec{k}\cdot\vec{r}) dA \right\} , \quad (207)$$

where $\vec{r}_o$ is the position of the observation point $\hat{k} = \vec{r}_o / |\vec{r}_o|$, $k = 2\pi/\lambda$, and $\vec{k} = k\hat{k}$. The first integral can be evaluated in closed form over each straight wire segment for the constant, sine, and cosine components of the basis functions, and reduces to a summation over the wire segments. With the surface current on each patch represented by a delta function at the patch center, the second integral becomes a summation over the patches.

The radiation pattern of an antenna can be computed by exciting the antenna with a voltage source and using equation (207) to compute the radiated field for a set of directions in space. Alternatively, since the transmitting and receiving patterns are required by reciprocity to be the same, the pattern can be determined by exciting the antenna with plane-waves incident from the same directions and computing the currents at the source point. The solution procedure in NEC does not guarantee reciprocity, however, since the different expansion and weighting functions may produce asymmetry in the matrix. Large differences between the receiving and transmitting patterns or a significant lack of reciprocity in bistatic scattering are indications of inaccuracy in the solution, possibly from too coarse a segmentation of the wires or surfaces.

The power gain of an antenna in the direction specified by the spherical coordinates (Θ,ϕ) is defined as

$$G_p(\Theta,\phi) = 4\pi \frac{P(\Theta,\phi)}{P_{in}} ,$$

where $P(\Theta,\phi)$ is the power radiated per unit solid angle in the direction (Θ,ϕ), and P_{in} is the total power accepted by the antenna from the source. P_{in} is computed from the voltage and current at the source as

$$P_{in} = \frac{1}{2} \mathrm{Re}(VI^*) \ ,$$

and

$$P(\Theta,\phi) = \frac{1}{2} R^2 \ \mathrm{Re}(\vec{E} \times \vec{H}^*) = \frac{R^2}{2\eta} (\vec{E} \cdot \vec{E}^*) \ .$$

$\vec{E}$ is obtained from equation (207) with $\vec{r}_o$ in the direction (Θ,ϕ), and $r_o = R$. Directive gain is similarly defined as

$$G_d(\Theta,\phi) = 4\pi \frac{P(\Theta,\phi)}{P_{rad}} \ ,$$

where P_{rad} is the total power radiated by the antenna,

$$P_{rad} = P_{in} - P_{loss} \ ,$$

and P_{loss} is the total ohmic loss in the antenna.

The radiated field of an antenna over ground is modified by the ground interaction, as discussed in section IV. When the range from the antenna to the observer, R, approaches infinity, the Sommerfeld formulation for the field reduces exactly to a direct field determined by equation (207) and a field from the image modified by the Fresnel reflection coefficient. In some cases, however, when the observer is at a finite distance from the antenna, the field components proportional to $1/R^2$ may be significant. While the $1/R$ terms are generally much larger than the $1/R^2$ terms at practical observation distances from an antenna, the $1/R$ terms vanish at grazing angles over an imperfect ground plane leaving only the $1/R^2$ terms, dominated by a term known as the ground wave. The ground wave is, of course, included in Sommerfeld's expressions. Norton's asymptotic approximations (ref. 26) are used, however, since they are more easily evaluated and give adequate accuracy. Norton's formulas, which are in Part II of this manual under subroutine GWAVE, are valid for R greater than a few wavelengths and to second order in k_1^2/k_2^2. When the ground wave is included, the field has radial as well as transverse components.

6. ANTENNA COUPLING

Coupling between antennas is often a parameter of interest, especially when a receiving system must be protected from a nearby transmitter. Maximum power transfer between antennas occurs when the source impedance and receiver load impedance are conjugate-matched to their antennas. Determination of this condition is complicated by the antenna interaction, however, since the input impedance of one antenna depends on the load connected to the other antenna. NEC-2 includes an algorithm for determining the matched loads and maximum coupling by a method that was added to special versions of the previous codes NEC-1 and AMP (ref. 34).

The coupling problem can be solved in closed form by the Linville method (ref. 35), a technique used in rf amplifier design. The first step is to determine the two-port admittance parameters for the coupled antennas by exciting each antenna with the other short-circuited and computing the self and mutual admittances from the currents computed by NEC. The maximum coupling is then

$$G_{MAX} = \frac{1}{L}\left[1 - (1-L^2)^{1/2}\right] ,$$

where

$$L = \frac{|Y_{12}Y_{21}|}{2\mathrm{Re}(Y_{11})\ \mathrm{Re}(Y_{22}) - \mathrm{Re}(Y_{12}Y_{21})} .$$

The matched load admittance on antenna 2 for maximum coupling is

$$Y_L = \left[\frac{1-\rho}{1+\rho} + 1\right] \mathrm{Re}(Y_{22}) - Y_{22} ,$$

where

$$\rho = \frac{G_{MAX}(Y_{12}Y_{21})^*}{|Y_{12}Y_{21}|} ,$$

and the corresponding input admittance of antenna 1 is

$$Y_{IN} = Y_{11} - \frac{Y_{21}Y_{12}}{Y_L + Y_{22}} .$$

References

1. Miller, E. K. et al., *Final Technical Report on the Log-Periodic Scattering Array Program,* MBAssociates Report No. MB-R-70/105, Contract No. F04701-68-C-0188, 1970.
2. *RCS Computer Program BRACT, Log-Periodic Scattering Array Program - II,* MBAssociates Report No. MB-R-69/46, Contract No. F04701-68-C-0188, 1969.
3. *Antenna Modeling Program - Composite User's Manual,* MBAssociates Report No. MB-R-74/46, 1974.
4. *Antenna Modeling Program - Engineering Manual,* MBAssociates Report No. MB-R-74/62, 1974.
5. *Antenna Modeling Program - Systems Manual,* MBAssociates Report No. MB-R-74/62, 1974.
6. *Antenna Modeling Program - Supplementary Computer Program Manual (AMP2),* MBAssociates Report No. MB-R-75/4, 1975.
7. *Numerical Electromagnetic Code (NEC-1) Part III: NEC User's Guide,* Lawrence Livermore Laboratory, 1977.
8. *Numerical Electromagnetic Code (NEC-1) Part II: NEC Program Description - Code,* Lawrence Livermore Laboratory, 1977.
9. Albertsen, N. C., Hansen, J. E., and Jensen, N. E., *Computation of Spacecraft Antenna Radiation Patterns,* The Technical University of Denmark, Lyngby, Denmark, June 1972.
10. Poggio, A. J. and Miller, E. K., "Integral Equation Solutions of Three-Dimensional Scattering Problems," Chapt. IV in *Computer Techniques for Electromagnetics,* edited by R. Mittra, Pergamon Press, New York, 1973.
11. Poggio, A. J. and Adams, R. W., *Approximations for Terms Related to the Kernel in Thin-Wire Integral Equations,* UCRL-51985, Lawrence Livermore Laboratory, CA, December 19, 1975.
12. Van Bladel, J., *Electromagnetic Fields,* McGraw-Hill, New York, 1964.
13. Harrington, R. F., *Field Computation by Moment Methods,* MacMillan, New York, 1968.
14. Yeh, Y. S. and Mei, K. K., "Theory of Conical Equiangular Spiral Antennas," *Part I - Numerical Techniques, IEEE Trans. Ant. and Prop., AP-15,* 1967, p. 634.

15. Neureuther, A. R. et al., "A Comparison of Numerical Methods for Thin Wire Antennas," *Presented at the 1968 Fall URSI Meeting,* Dept. of Electrical Engineering and Computer Sciences, University of California, Berkeley, 1968.

16. Miller, E. K. et al., *An Evaluation of Computer Programs Using Integral Equations for the Electromagnetic Analysis of Thin Wire Structures,* UCRL-75566, Lawrence Livermore Laboratory, CA, March 1974.

17. Wu, T. T. and King, R. W. P., "The Tapered Antenna and Its Application to the Junction Problem for Thin Wires," *IEEE Trans. Ant. and Prop., AP-24,* No. 1, pp. 42-45, January 1976.

18. Poggio, A. J., *Integral Representations for Fields Due to Sources on Open Surfaces with Applications to End Caps,* UCRL-51723, Lawrence Livermore Laboratory, CA, December 16, 1974.

19. Ralston, A., *A First Course in Numerical Analysis,* McGraw-Hill, New York 1965.

20. Sommerfeld, A., *Partial Differential Equations in Physics,* Academic Press, New York, 1964.

21. Burke, G. J., Miller, E. K., and Poggio, A. J., *Dielectric Ground Interactions with a Log-Periodic Antenna,* Final Report, ECOM-0285-F, U.S. Army Electronics Command, Fort Monmouth, N.J., 1971 (contract DAAB07-70-C-0285).

22. Miller, E. K., Poggio, A. J., Burke, G. J., and Selden, E. S., *Analysis of Wire Antennas in the Presence of a Conducting Half Space: Part I. The Vertical Antenna in Free Space. Part II. The Horizontal Antenna in Free Space,* UCRL-73217, Lawrence Livermore Laboratory, CA, 1972. (Also in *Canadian J. Phys.*)

23. Lager, D. L. and Lytle, R. J., *Fortran Subroutines for the Numerical Evaluation of Sommerfeld Integrals Unter Anderem,* UCRL-51821, Lawrence Livermore Laboratory, CA, May 21, 1975.

24. Adams, R. W., Poggio, A. J., and Miller, E. K., *Study of a New Antenna Source Model,* UCRL-51693, Lawrence Livermore Laboratory, CA, October 28, 1974.

25. Brittingham, J. N., Miller, E. K., and Okada, J. T., *SOMINT: An Improved Model for Studying Conducting Objects Near Lossy Half-Spaces,* UCRL-52423, Lawrence Livermore Laboratory, CA, February 24, 1978.

26. Norton, K. A., "The Propagation of Radio Waves Over the Surface of the Earth and in the Upper Atmosphere," *Proceedings of the Institute of Radio Engineers,* Vol. 26, No. 9, Sept. 1937.

27. Lytle, R. J. and Lager, D. L., *Numerical Evaluation of Sommerfeld Integrals,* UCRL-51688, Lawrence Livermore Laboratory, CA, October 23, 1974.

28. Shanks, D., "Non-Linear Transformations of Divergent and Slowly Convergent Sequences," *J. Math. Phys.,* 24, 1 (1955).

29. Miller, E. K. and Deadrick, F. J., *Computer Evaluation of Loran-C Antennas,* UCRL-51464, Lawrence Livermore Laboratory, CA, Oct. 17, 1973.

30. Wait, J. R., "Characteristics of Antennas Over Lossy Earth," *Antenna Theory, Part II,* R. E. Collin and F. J. Zucker, Eds., McGraw-Hill, New York, pp. 386-437, 1969.

31. King, R. W., *The Theory of Linear Antennas,* Harvard Univ. Press, Cambridge, Massachusetts, 1956.

32. Otto, D. V., "The Admittance of Cylindrical Antennas Driven from a Coaxial Line," *Radio Sci.,* Vol. 2, No. 9, pp. 1031-1042, 1967.

33. Andreasen, M. G. and Harris, F. G., *Analyses of Wire Antennas of Arbitrary Configuration by Precise Theoretical Numerical Techniques,* Tech. Rept. ECOM 0631-F, Granger Associates, Palo Alto, California, Contract DAAB07-67-C-0631, 1968.

34. Logan, J. C. and Rockway, J. W., *Computer Techniques for Shipboard Topside Antenna Modeling Below UHF,* TN-3284, Naval Electronics Laboratory Center, November 17, 1976.

35. Rubin, D., *The Linville Method of High Frequency Transistor Amplifier Design,* Naval Weapons Center, Research Department, NWCCL TP 845, Corona Laboratories, Corona, California, March 1969.

36. Burke, G. J. and Poggio, A. J., *Computer Analysis of the Twin-Whip Antenna,* UCRL-52080, Lawrence Livermore Laboratory, CA, June 1, 1976.

37. Burke, G. J. and Poggio, A. J., *Computer Analysis of the Bottom-Fed Fan Antenna,* UCRL-52109 Lawrence Livermore Laboratory, CA, August 19, 1976.

38. Deadrick, F. J., Burke, G. J., and Poggio, A. J., *Computer Analysis of the Trussed-Whip and Discone-Cage Antennas,* UCRL-52201, January 6, 1977.

RAC/gw